Pushing the Limits of Large Language Model Quantization via the Linearity Theorem

Vladimir Malinovskii[†]
Yandex, HSE University

Andrei Panferov[†]
ISTA[▽]

Ivan Ilin
GenAI CoE, KAUST[*]

Han Guo
MIT[◇]

Peter Richtárik
GenAI CoE, KAUST[*]

Dan Alistarh
ISTA[▽], NeuralMagic

Abstract

Quantizing large language models has become a standard way to reduce their memory and computational costs. Typically, existing methods focus on breaking down the problem into individual layer-wise sub-problems, and minimizing per-layer error, measured via various metrics. Yet, this approach currently lacks theoretical justification and the metrics employed may be sub-optimal. In this paper, we present a "linearity theorem" establishing a direct relationship between the layer-wise ℓ_2 reconstruction error and the model perplexity increase due to quantization. This insight enables two novel applications: (1) a simple *data-free LLM quantization method using Hadamard rotations and MSE-optimal grids*, dubbed HIGGS, which outperforms all prior data-free approaches such as the extremely popular NF4 quantized format, and (2) an *optimal* solution to the problem of finding non-uniform per-layer quantization levels which match a given compression constraint in the medium-bitwidth regime, obtained by reduction to dynamic programming. On the practical side, we demonstrate improved accuracy-compression trade-offs on Llama-3.1 and 3.2-family models, as well as on Qwen-family models. Further, we show that our method can be efficiently supported in terms of GPU kernels at various batch sizes, advancing both data-free and non-uniform quantization for LLMs.

1 Introduction

Quantization has become a standard technique for reducing the memory costs of large language models (LLMs), e.g. (Dettmers et al., 2022; Dettmers and Zettlemoyer, 2022; Frantar et al., 2022; Lin et al., 2023; Chee et al., 2023; Tseng et al., 2024a; van Baalen et al., 2024). Most existing high-performance approaches start from the natural strategy of quantizing layers one-at-a-time, while minimizing a given per-layer error function, such as per-layer quantization entropy (Dettmers et al., 2023a) or ℓ_1-norm error (Yoshida, 2023).

In this context, a reasonable question regards the relationship between *the individual per-layer quantization error*, measured in terms of, e.g., output MSE, and *the model's output error*, measured in terms of, e.g., validation perplexity (PPL). While previous work observes that various layers can have vastly different "sensitivities" towards the model's output (Yin et al., 2024; Frantar and Alistarh, 2022), it is currently not clear how these can be estimated. Moreover, it is not clear what the correct error metric quantization techniques should be minimizing.

Contribution. In this paper, we start by examining the relationship between per-layer error and global error from the theoretical perspective, and identify a natural "linearity theorem", which precisely links the model's performance in terms of output loss (or PPL), with the per-layer MSE quantization error over the weights. Roughly speaking, we show that, for reasonable quantization bit-widths, the relationship between per-layer MSE and output PPL is *linear*, modulo a *constant* scaling coefficient per layer, which is *independent of the quantization approach*. We show experimentally that the theorem works remarkably well at predicting quantization error for different schemes in the 3-8 bit range; see Figure 1 for an illustration.

The linearity theorem, whose technical prerequisites and complete proof we provide, has a few non-trivial practical implications. First, it guides us towards a state-of-the-art *data-free* quantization method. Specifically, we start by observing that, for a fixed per-layer compression budget, the linearity theorem implies that minimizing the perplexity increase can be reduced to minimizing

[†] Equal contribution
[◇] Massachusetts Institute of Technology
[▽] Institute of Science and Technology Austria
[*] King Abdullah University of Science and Technology, Saudi Arabia

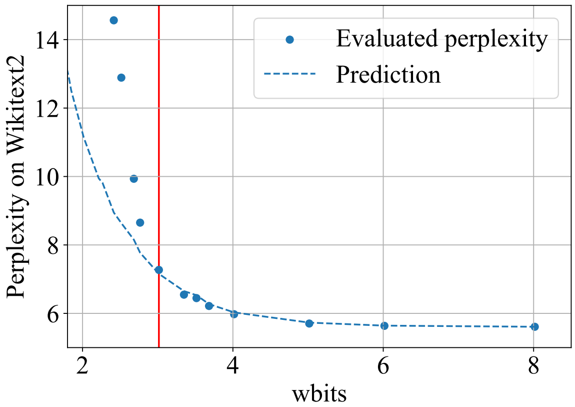

Figure 1: Actual *measured* Perplexity (PPL) of quantized models versus *predicted* PPL, following Theorem 1, for uniform HIGGS quantization of Llama 3.1 8B in the 2–8 bit range. Vertical line shows the limit of the theorem's applicability

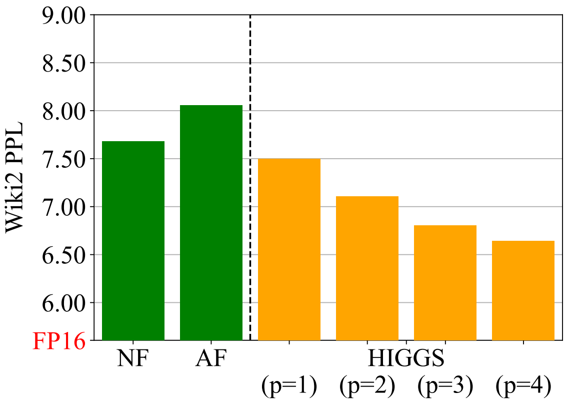

Figure 2: Comparison of Normal Float (NF), Abnormal Float (AF) and HIGGS on Llama 3.1 8B quantization to 3.19-3.25 bitwidth range. HIGGS is instantiated at different lattice dimensionalities p.

the individual, per-layer MSE quantization errors. Moreover, we observe that we can do this in a *calibration-free* fashion if the model weights are incoherence-processed via Hadamard rotations—known to make them approximately Gaussian—and then we quantize using Gaussian-MSE-optimal grids, which are efficiently computable (Pagès and Printems, 2003). The resulting method, called HIGGS (for Hadamard Incoherence with Gaussian MSE-optimal GridS) is highly accurate and efficiently implementable for various bit-widths and grid constraints.

The second practical application of the linearity theorem comes for solving the *non-uniform quantization* problem: that is, the problem of finding the per-layer bit-widths which satisfy a fixed constraint on the total model size / average bits per parameter, which minimize the perplexity increase. In the range of applicability of the linearity theorem, we show that optimal non-uniform compression can be reduced to knapsack-style dynamic programming over the set of quantization choices at each layer. Interestingly, in this range, this problem can be solved *optimally* using existing linear programming solvers; in practice, solving an LLM-sized instance can be done in seconds. While this procedure requires computation of the per-layer linear scaling coefficients, we show that this can be done efficiently and even *data-free*, based on randomly sampled input token sequences. Moreover, interestingly, the two applications can be compounded, yielding an *optimal non-uniform data-free* quantization technique, which we call *dynamic HIGGS*.

We validate our practical applications experimentally by quantizing the popular Llama 3.1 and Llama 3.2 models (Dubey et al., 2024), as well as a Qwen model (Bai et al., 2023), across a wide range of bit-widths, and evaluating on standard perplexity (PPL) and in-context learning (ICL) benchmarks. The results, sampled in Figure 2, confirm the fact that HIGGS with uniform quantization can outperform the Normal Float (NF) and Abnormal Float (AF) formats for lower bit-widths in the 3-4 bit range, as well as the recent data-free HQQ method (Badri and Shaji, 2023). At the same time, for higher bitwidths, we observe that all methods produce results in the same accuracy range. The *dynamic, non-uniform* variant of HIGGS provides consistent additional accuracy boosts, and appears to lead state-of-the-art results for quantization methods with efficient hardware support. Surprisingly, we observe that dynamic HIGGS can even outperform *calibration-based* methods such as GPTQ (Frantar et al., 2022) and AWQ (Lin et al., 2023) in the 3-4 bit-width range. Moreover, HIGGS can be applied in conjunction with GPTQ, leading to state-of-the-art accuracy results for scalar quantization.

On the runtime side, we show that our approach can be supported extremely efficiently via GPU kernels. Specifically we show that the recent FLUTE kernel design (Guo et al., 2024) can be adapted to support a subset HIGGS multi-dimensional grids, providing a high accuracy solution that is efficient across various batch sizes. Our solution can be integrated with both Pytorch (Paszke et al., 2019) and vLLM (Kwon et al., 2023), leading to speedups of

2-3x relative to FP16 precision, at a low decrease in accuracy relative to the FP16 baseline.

2 Background and Related Work

Post-training quantization (Nagel et al., 2020; Gholami et al., 2021) of LLMs has become an extremely active research area. Here, we provide some background, focusing on the work closest to ours. The focus of early work in LLM quantization has been on *data-free* methods (Dettmers et al., 2022; Yao et al., 2022; Park et al., 2022) using direct round-to-nearest (RTN) quantization over small weight groups. For example, given a group of g consecutive layer weights, viewed as a vector $\mathbf{x} \in \mathbb{R}^g$, we define b-bit RTN as

$$\begin{aligned} \mathcal{Q}(\mathbf{x}, b) &= \mathrm{rnd}\left(\frac{\mathbf{x} - \min(\mathbf{x})}{\max(\mathbf{x}) - \min(\mathbf{x})}(2^b - 1)\right) \\ &= \mathrm{rnd}((\mathbf{x} - z(\mathbf{x}))/s(\mathbf{x})), \end{aligned} \tag{1}$$

where rnd rounds to the nearest integer level, $z = z(\mathbf{x}) = \min(\mathbf{x})$ is the "zero point" and $s = s(\mathbf{x}) = (\max(\mathbf{x}) - \min(\mathbf{x}))/(2^b - 1)$ is the min-max scale.

One key issue with this first wave of data-free RTN methods is that they tend to yield high accuracy loss below 8 bits per parameter. This can be addressed primarily in two ways: (1) by improving the rounding function in a *data-aware* way, and (2) by using more complex *non-uniform grids*.

Data-Aware Methods. Calibration-based methods such as GPTQ (Frantar et al., 2022) improved significantly upon RTN by allowing a subset of weights to be adjusted during quantization, based on a sample of calibration data. Follow-up methods such as AWQ (Lin et al., 2023), SqueezeLLM (Kim et al., 2023), OWQ (Lee et al., 2024) and SpQR (Dettmers et al., 2023b) implemented variants of outlier-aware quantization, where a small fraction of weights are effectively stored in higher precision. Further, high-compression methods such as QuIP (Chee et al., 2023), QuIP# (Tseng et al., 2024a), QTIP (Tseng et al., 2024b) and AQLM (Egiazarian et al., 2024) investigated much more complex quantized representations, such as lattice quantization, often paired with incoherence pre-processing of the weights, and GPTQ-like weight updates. While such methods can be Pareto-competitive down to 2 bits per parameter, some practical disadvantages are 1) the reliance on task-specific calibration data, 2) the relatively high processing time to produce models, as well as 3) the complexity of efficiently supporting lattice representations at runtime.

We emphasize the fact that the linearity theorem has no direct bearing on the *data-aware* layer-wise MSE minimization problems considered in references such as GPTQ and QuIP, which are of the form

$$\min_{\widehat{W}_l \in \Omega_l} \|W_l^\star X - \widehat{W}_l X\|_F^2,$$

where $W_l^\star$ is a matrix of pre-trained weights corresponding to layer l, $\widehat{W}_l = \mathcal{Q}_l(W_l^\star)$ represents the quantized weights, X represents the layer's input, Ω_l represents the collection of feasible/allowed quantized matrices, and $\|\cdot\|_F$ is the Frobenius norm. Here, we focus on the data-free case, and relate it to the quantization MSE over weights.

Data-free Non-Uniform Quantization. To address the limitations of calibration-based methods, highly-popular open-source LLM inference frameworks such as `bitsandbytes` (`BNB`) (Dettmers and von Koeller, 2021) employ *data-free* quantization, but under optimized *non-uniform* grids, designed to reduce reconstruction error. Specifically, Dettmers et al. (2023a) proposed Normal Float (NF) grids which minimize *quantization entropy*, while Abnormal Float (AF) (Yoshida, 2023), optimizes ℓ_1 reconstruction error, arguing that it leads to better accuracy than NF. To optimize for those quantities, these works assume that LLM weights follow a *zero-mean Gaussian distribution*, but do not enforce this assumption in any way. HQQ (Badri and Shaji, 2023) provides and data-free algorithm to optimize the scale and zero-point for *uniform* grids, while FLUTE (Guo et al., 2024) provides efficient GPU support for 1D non-uniform grids such as those of NF.

Recent work on data-aware methods (Chee et al., 2023; Tseng et al., 2024a; Ashkboos et al., 2024; Liu et al., 2024) applies *incoherence pre-processing* to the weights, often in the form of Hadamard transforms, to enforce a better match between the distribution of processed weights and the Gaussian. Yet, surprisingly, incoherence has so far only been used in the context of *data-aware* and *uniform-grid* quantization methods.

Our work starts from a simple and general way of linking per-layer compression error with the global model loss increase. This inspires two different applications to data-free and non-uniform quantization, which are complementary to the aforementioned work.

Additional Related Work. The combination of Hadamard preprocessing and Gaussian MSE-optimal grids has also been proposed for *gradient compression* in distributed optimization (Vargaftik et al., 2021, 2022; Davies et al., 2020). Gaussian MSE-optimal grids have been applied to multi-dimensional numerical integration by Pagès and Printems (2003). From them, we borrow the CLVQ algorithm for optimal grid computation given a set of parameters.

3 The Linearity Theorem

This section provides an overview of the linearity theorem, which links the layer-wise L2 error induced by quantization, to the increase in model perplexity, providing a theoretical foundation for weight quantization methods.

3.1 Notation

Pre-trained model. Let $W^\star := (W_1^\star, \ldots, W_L^\star)$, where for each l in the set $\{1, \ldots, L\}$, by $W_l^\star \in \mathbb{R}^{d_{in}^l \times d_{out}^l}$ we denote the matrix representing a linear layer of the pre-trained model we are interested in compressing/quantizing.

Reshaping operator. Given a layer index l, let $\mathcal{R}_l : \mathbb{R}^{d_{in}^l \times d_{out}^l} \to \mathbb{R}^{d_{in}^l \cdot d_{out}^l}$ be the "reshaping" operator, reshaping a matrix into a large-dimensional vector. That is, $\mathbf{w}_l = \mathcal{R}_l(W_l)$ is the vector obtained from the matrix W_l by concatenating entries of W_l into a single $d^l := d_{in}^l \times d_{out}^l$ dimensional vector. The entries can be concatenated in any order as long as it is always fixed. Note that $\|W_l\|_F = \|\mathcal{R}_l(W_l)\|_2 = \|\mathbf{w}_l\|_2$. Further, let $\mathcal{R}_l^{-1}$ be the inverse reshaping operator mapping $\mathbf{w}_l$ back to W_l, such that $\mathcal{R}_l^{-1}(\mathbf{w}_l) = \mathcal{R}_l^{-1}(\mathcal{R}_l(W_l)) = W_l$. Let $\mathbf{w} := (\mathbf{w}_1, \ldots, \mathbf{w}_L) \in \mathbb{R}^d$, where $d := \sum_{l=1}^L d^l$, and $\mathcal{R}^{-1}(\mathbf{w}) := (\mathcal{R}_1^{-1}(\mathbf{w}_1), \ldots, \mathcal{R}_L^{-1}(\mathbf{w}_L))$. Define $\mathcal{R}$ in a similar manner, and let $\mathbf{w}^\star := \mathcal{R}(W^\star)$ be the "vector" representation of the pre-trained model in $\mathbb{R}^d$.

Perplexity. Let $\phi : \mathbb{R}^d \to \mathbb{R}$ be the perplexity function on $\mathbb{R}^d$ defined formally as

$$\phi(\mathbf{w}) := PPL(\mathcal{R}^{-1}(\mathbf{w})),$$

where PPL is the perplexity function operating in the space of W.

3.2 Technical Assumptions

Our results hold under the following assumptions, which we describe and discuss below.

Assumption 1 (Local optimality of the pre-trained weights). *The* uncompressed model weights $\mathbf{w}^\star$ *are a local minimizer of perplexity* ϕ*.*

It is easy to see that if $W^\star$ is a local minimizer of PPL if and only if $\mathbf{w}^\star = \mathcal{R}(W^\star)$ is a local minimizer of ϕ. We emphasize that Assumption 1 is not needed if the compression mechanism used to compress each matrix $W_l^\star$ is unbiased, i.e., if $\mathrm{E}\left[\widehat{W}_l\right] = W_l^\star$ for all $l \in \{1, \ldots, L\}$. We will leverage this observation in Section 5.

Assumption 2 (Local smoothness of perplexity)**.** *The perplexity function* ϕ *is three times continuously differentiable in a neighborhood of* $\mathbf{w}^\star$.

Recall that $W^\star = (W_1^\star, \ldots, W_L^\star)$ represents the pre-trained weights. Let $D_l^\star := \|W_l^\star\|_F I_{d_l} \in \mathbb{R}^{d_l \times d_l}$ for $l \in \{1, \ldots, L\}$, and

$$D^\star := Diag(D_1^\star, \ldots, D_L^\star) \in \mathbb{R}^{d \times d},$$

where I_{d_l} is the $d_l \times d_l$ indentity matrix.

Assumption 3 (Regularity of pre-trained weights)**.** *There exists a block-diagonal matrix* $Z = Diag(Z_1, \ldots, Z_L)$*, where* $Z_l = z_l I_{d_l}$*,* $z_l > 0$ *for all* $l \in \{1, \ldots, L\}$*, such that*

$$D^\star \nabla^2 \phi\left(\mathcal{R}(W^\star)\right) D^\star \approx Z. \tag{2}$$

Discussion. If ϕ is twice differentiable (which is implied by Assumption 2), and $\mathbf{w}^\star$ is a local minimizer of ϕ (see Assumption 1), then the Hessian $\nabla^2\phi(\mathbf{w}^\star)$ is necessarily positive semi-definite. Clearly, $D^\star$ is diagonal with non-negative entries, and hence it is positive semi-definite. Therefore, $D^\star \nabla^2 \phi\left(\mathcal{R}(W^\star)\right) D^\star$ is also positive semi-definite. Let $\lambda_{\min}$ (resp. $\lambda_{\max}$) be the smallest (resp. the largest) eigenvalue of $D^\star \nabla^2 \phi\left(\mathcal{R}(W^\star)\right) D^\star$. Then

$$\lambda_{\min} I_d \preceq D^\star \nabla^2 \phi\left(\mathcal{R}(W^\star)\right) D^\star \preceq \lambda_{\max} I_d.$$

We validate that Assumption 3 holds on language models in Appendix E.

3.3 Theorem Statement

With this in place, we can now state our result.

Theorem 1 (Linearity theorem)**.** *Let the above assumptions hold. Given an arbitrary layer index* l *and an arbitrary (possibly stochastic) quantizer function* $\mathcal{Q}_l$*, let* $\widehat{W}_l := \mathcal{Q}_l(W_l^\star)$ *be the compressed version of the layer weights* $W_l^\star$*. For each layer* l*, define the parameter* t_l *as the relative quantization error, i.e.:*

$$t_l^2 = t_l^2(W_l, \mathcal{Q}_l) := \frac{\mathrm{E}\left[\|\widehat{W}_l - W_l^\star\|_F^2\right]}{\|W_l^\star\|_F^2}, \tag{3}$$

Then, as long as $t_1, \ldots, t_L$ are small enough, the following linear approximation of the expected perplexity holds:

$$\mathrm{E}\left[PPL(\widehat{W})\right] \approx PPL(W^\star) + \sum_{l=1}^{L} \alpha_l t_l^2, \qquad (4)$$

where expectation is taken w.r.t. the randomness in the compression process, and the terms α_l are layer specific constants that are independent of the compression process.

Discussion. The proof of the above result can be found in Appendix D. The result essentially says that, given an *arbitrary* (possibly randomized) perturbation function applied over the weights, if we can compute bounds t_l on the (relative) Frobenius norm of the perturbation at each layer, then there exist layer-wise constant coefficients α_l such that the linear approximation of the global perplexity increase in Eqn. (4) holds. Importantly, the coefficients α_l are "universal," in the sense that their values depend only on the layer weights, and not on the quantization function. In the following, we will explore two of its practical implications.

4 HIGGS: Hadamard Incoherence and Gaussian MSE-Optimal Grids

4.1 The Hadamard Incoherence Trick

Theorem 1 defines two sets of coefficients for each layer l: (1) The *error coefficients* t_l, which measure the error relative to the layer's norm; and (2) The *scaling coefficients* α_l measuring the importance of the per-layer error towards the output.

Imagine that we would wish to compute these coefficients, in order to upper bound the compression error. One key issue is that, while the scaling coefficients α_l are compression-independent, the error coefficients $t_l = t_l(W_l^\star, \mathcal{Q}_l)$ defined in Eqn. (3) are specific to both the layer being compressed and *to the quantizer used for compression*.

However, we can *remove this weight distribution dependence of the t_l coefficients* by applying preprocessing to the weights. Specifically, it is well-known (Ailon and Chazelle, 2009; Suresh et al., 2017; Chee et al., 2023) that multiplication of the layer weights with the Random Hadamard Transform (RHT) leads the weight distribution to closely match a Gaussian distribution, *independently of the original weights*.

Specifically, let us assume that we are applying the RHT to the weights, and then rounding to an arbitrary grid $\mathcal{G}_n^p$. The exact procedure is described in Algorithm 1. Since, post-RHT, the weight distribution is approximately Gaussian, we obtain that, in this case, the layer error coefficients t_l will only depend on the chosen grid, and *not on the original weights*. (Please see the proof of this fact in Appendix F.) More specifically, t_l^2 approximately equals the per-dimension MSE of rounding the multivariate standard normal distribution to the grid $\mathcal{G}_n^p$, **which is constant given n and p, and independent of the original weights**.

In this context, Theorem 1 implies that if weights are Hadamard-transformed, then **MSE-optimized grids should be theoretically-optimal in terms of end-to-end model error**, given a fixed bit budget.

In the following subsection, we detail and expand these observations.

4.2 MSE-optimal grids for LLM quantization

Our previous insights lead to a simple alternative to Normal Float (NF) and Abnormal Float (AF) grids: after Hadamard rotations, we can quantize to a grid minimizing the $L2$ (MSE) quantization error. We call this approach **H**adamard **I**ncoherence and **G**aussian MSE-optimal **G**rid**S** (HIGGS). The algorithm combines the following components to achieve minimal quadratic quantization error: 1) Hadamard preprocessing of the quantized weights, 2) multi-dimensional (vector) quantization, and 3) Gaussian MSE-optimal quantization grids.

Section 4.1 described the exact quantity we need to optimize when choosing $\mathcal{G}_n^p$: the expected MSE of rounding the multivariate Normal distribution to $\mathcal{G}_n^p$. This problem has a rich history, and it can be solved optimally by the Pagès and Printems (2003) algorithm arising in numerical PDEs. We use the same grid optimization procedure, as well as some pre-computed optimal grids. Applying those grids to Algorithm 1 constitutes Algorithm 2. It important to note that the optimal grid only has to be computed once for any pair of n and p.

To validate HIGGS, we compare it with other quantization grids, namely Normal Float (NF) (Dettmers et al., 2023a) and Abnormal Float (AF) (Yoshida, 2023). The results, sampled in Figure 2, indicate that HIGGS outperforms other grids in terms of output perplexity on WikiText-2 (Merity et al., 2016a). A more detailed comparison, including more baselines as well as zero-shot and few-shot tasks for both low and high bitwidth quantization can be found in Table 3.

Algorithm 1 Vector Quantization with Random Hadamard Transform (RHT-VQ)

```
    Parameters: grid $\mathcal{G}_n^p$ of $n$ elements of dimension $p$, scales group size $g$ that is a power of 2.
    Input: vector $\mathbf{w} = (\mathbf{w}_{\{1\}}, \dots, \mathbf{w}_{\{D/g\}}) \in \mathbb{R}^D$, RHT seed $\xi$.
    Output: quantized vector $\mathbf{q}^\dagger \in \{1, 2, \dots, n\}^{D/p}$, scales vector $\mathbf{s} \in \mathbb{R}^{D/g}$.
  Sequentially partition $\mathbf{w} \in \mathbb{R}^D$ into $D/g$ subvectors $\mathbf{w}_{\{i\}} \in \mathbb{R}^g$, where $i = 1, \dots, D/g$
  for $i = 1, \dots, D/g$ do
      $s_i = \|\mathbf{w}_{\{i\}}\|_2$
      $\mathbf{w}^\dagger_{\{i\}} = \mathit{RandomHadamardTransform}(\mathbf{w}_{\{i\}}/s_i, \xi)$   ▷ entries of $\mathbf{w}^\dagger_{\{i\}}$ are approx. from $\mathcal{N}(0,1)$
      $\mathbf{q}^\dagger_{\{i\}} = \mathit{RoundToNearest}(\mathbf{w}^\dagger_{\{i\}}, \mathcal{G}_n^p)$   ▷ Projecting $d$ sequential values together
  end for
  $\mathbf{q}^\dagger = \left[\mathbf{q}^\dagger_{\{1\}}, ..., \mathbf{q}^\dagger_{\{D/g\}}\right]$   ▷ † signifies that the vector is in Hadamard transformed space
  $\mathbf{s} = \left[s_1, ..., s_{D/g}\right] / \sqrt{g}$
```

Algorithm 2 HIGGS Algorithm

```
    Parameters: grid dimensions $n$ and $p$, scales group size $g$ that is a power of 2.
    Input: Algorithm 1 input.
    Output: Algorithm 1 output.
  $\mathcal{G}_n^p = \texttt{CLVQ}(n, p)$ ▷ (Pagès and Printems, 2003), computed once
  $(\mathbf{q}^\dagger, \mathbf{s}) = \texttt{RHT-VQ}(\mathcal{G}_n^p, g, \mathbf{w}, \xi)$   ▷ Algorithm 1
```

4.3 Practical Configurations

HIGGS has a number of hyperparameters: the grid size n, the grid dimension p and the group size g. Varying those, we can, in theory, achieve any per-parameter bitwidth. However, a number of practical considerations apply if we consider setups that can be efficiently implemented in practice:

Constraint 1: To optimize memory efficiency, n must be a power of 2. Since most modern architectures support data types with a minimum granularity of 1 byte (8 bits), it is advantageous if $\log_2(n)$ is a multiple of 8. When $\log_2(n)$ is less than 8 but is still a power of 2 (e.g., n=4, 16), standard bit-packing methods can be used effectively. However, for cases where $\log_2(n)$ is not a power of 2 (e.g., n=8, 64), the data can be efficiently managed by partitioning it into multiple sections or bit-slices (Xia et al., 2024).

Constraint 2: Grid memory access patterns can be sporadic. The ability to store the whole grid in low-latency memory would improve the performance of both decoding and matrix-multiplication operations. On modern GPUs, taking into account the usual shared-memory size of around 128Kb and $\frac{32}{k}\times$ replication to avoid bank conflicts, that would mean that the total number of points in the grid $2^{k\times p}$ can be at most $\approx 2^{10}$. Increasing the grid dimension at fixed bitwidth reduces the expected error, as seen in Figure 2. This limitation creates a quantization error lower bound dictated by which dimensions we can use in practice.

The quantized matrix can be either restored via the Inverse Hadamard Transform or processed in the transformed space directly with virtually no matrix multiplication complexity overhead. (Refer to Appendix G for theoretical and practical justification). Moreover, the Hadamard Transform functionality can be fully isolated from the matrix multiplication itself, allowing us to reuse existing lookup-table-based kernels for the latter.

FLUTE kernel. LLM decoding is typically memory-bound in the low-batch regime, making a GPU kernel that fuses dequantization and GEMM essential for achieving practical performance gains. A key component of such a fused HIGGS kernel is a primitive for vectorized indexing into the grid, implemented via a lookup table. The problem of implementing such kernel has been extensively studied by Guo et al. (2024), resulting in their developing FLUTE: a scalar lookup table matrix multiplication kernel. FLUTE efficiently stores the lookup table in the GPU's shared memory, enabling faster on-chip memory access. Moreover, it efficiently optimizes the dot product computation patterns speeding up the processing of larger batch sizes.

The simplicity of the HIGGS design makes it compatible with FLUTE out of the box for grids where $p = 1$. By adapting the kernels for vectorized lookups, we were able to unlock this functionality also for $p = 2$. This extension allows us to handle vector-quantized data, supporting configurations $p \in \{1, 2\}$ and $b \in \{2, 3, 4\}$. In practice, $p = 2$ is always preferable to $p = 1$. We will refer to those setups as FLUTE grids.

Table 1 demonstrates the performance of the FLUTE lookup table approach for HIGGS ($p = 2$), relative to MARLIN (Frantar et al., 2024) uniform quantization, Normal Float (NF) (Dettmers et al., 2023a), AQLM (Egiazarian et al., 2024) and the

QTIP (Tseng et al., 2024b) specialized trellis quantized matrix multiplication kernels. For the QTIP and FLUTE kernels, these measurements already include the cost of the underlying Hadamard transforms. As we can see, FLUTE kernels achieve the best performance across a variety of bitwidths and batch sizes.

Constrained HIGGS. To extend our method to higher bitwidths not supported by FLUTE (e.g. 8bit), we propose to reuse the existing uniform quantized matrix multiplication kernels (Wang et al., 2024; torchao maintainers and contributors, 2024). To bridge the gap between HIGGS and those kernels in this high-density setting, we constrain the HIGGS grid to be uniform, essentially solving for positioning and scaling of uniform grids to minimize expected MSE over the Gaussian distribution. Such grids might be suboptimal in terms if MSE, but make up for it in terms of kernel support. In practice, we use this trick to allow for $p = 1$, $b = 8$ inference, to which we will refer as CH8.

4.4 Application to GPTQ

HIGGS can naturally be used in more sophisticated rounding schemes that utilize layer activations information to achieve smaller effect of quantization on model performance (1-shot quantization methods). Extension to GPTQ (Frantar et al., 2022), one of the most popular such methods, in the form as we propose it can quickly be described as replacing the $RoundToNearest$ operation in Algorithm 1 with a different rounding operator that takes layer activations information into account. The resulting 1-shot quantized weights are structurally identical those obtained from Algorithm 1.

In Table 2, we present comparison of original GPTQ (Frantar et al., 2022), AQLM (Egiazarian et al., 2024), QuIP# (Tseng et al., 2024a), QTIP (Tseng et al., 2024b) the and GPTQ extension of HIGGS (for details on this scheme, see Appendix H). Although the latter does not outperform the more complicated quantization schemes such as AQLM, QuIP# and QTIP, we note that these methods use a more complex representation, and therefore provide very limited kernel support due to complexity of these representations. The GPTQ extension of HIGGS, on the other hand, can be mapped to FLUTE kernels (Guo et al., 2024) achieving high throughput at a variety of setups. The full results can be examined in Table 1, showing that we can reach close to 3x speedups in some configurations, and that this speedup is consistent across batch sizes from 1 to 16.

Algorithm 3 Error coefficient calibration

```
    Input: Calibration constants $t_1, \dots, t_J$; pre-trained model $W^\star = (W^\star_1, \dots, W^\star_L)$
    Output: linear coefficients $\alpha_1, \dots, \alpha_L$
  for $l = 1, \dots, L$ do
      for $j = 1, \dots, J$ do
          $\Delta_{l,j} = PPL(W^\star(l, t_j)) - PPL(W^\star)$
      end for
      $\alpha_l = \arg\min_{\alpha'_l} \sum_{j=1}^{J} \left(\Delta_{l,j} - \alpha'_l \cdot t_j^2\right)^2$
  end for
```

5 Variable Bitwidth Quantization

The second application of the Linearity Theorem is in *dynamic* quantization, i.e. choosing per-layer quantization bitwdiths that best reflect the “sensitivity” of different layers to quantization. Here, we leverage the observation that uniform biwidth compression might be far from optimal in terms of output error (Yin et al., 2024). Finding the optimal configuration is challenging due to exponentially-many possible solutions. We show that our quantization error model can efficiently find the optimal configuration for any target bitwidth, without having to evaluate all possible configurations.

Discrete Optimization Formulation. Assume a natural setting in which we wish to quantize each layer $W^\star_l$ using one quantizer from a finite set of options $\{\mathcal{Q}_1, \dots, \mathcal{Q}_J\}$, each with its own error. Let $j_l \in \{1, \dots, J\}$ denote the selection of the quantizer for layer l. Assume that quantizer $\mathcal{Q}_{j_l}$ corresponds to a specific bitwidth b_{j_l} and specific induced error t^2_{l,j_l} from Eqn. (3). We wish to find the optimal assignment *minimizing perplexity error*, while matching a specific average bitwidth $b_{\max}$.

Problem Formulation. Using error linearity from Theorem 1, and the coefficients $\alpha_1, \dots, \alpha_L$ estimated via Algorithm 3 as an input, this minimization problem can be written as

$$\begin{gathered} \min_{j_1,\dots,j_L} \sum_{l=1}^{L} \alpha_l \cdot t^2_{l,j_l} \\ \sum_{l=1}^{L} b_{j_l} \cdot d^l \le b_{\max} \cdot d \\ j_l \in \{1, \dots, J\} \text{ for all } l \in \{1, \dots, L\} \end{gathered} \tag{5}$$

where $b_{\max}$ is the target bitwidth. Recall that $d := \sum_{l=1}^{L} d^l$.

Estimating Scaling Coefficients. Theorem 1 shows that the scaling coefficients α_l do *not* depend on the quantization method used. We use this

Table 1: End-to-end throughput (tok/s, higher is better) comparison of quantized matrix multiplication kernels for Llama-3.1-8B at different bitwidths and batch sizes on an NVIDIA RTX 4090 GPU. We observe that MARLIN (which only supports uniform grids) and FLUTE are the only approaches that support speedups are batch sizes larger than 1, relative to FP16.

batch size	1			4			16		
FP16	57			224			862		
kernel \ wbits	2	3	4	2	3	4	2	3	4
MARLIN	-	-	133	-	-	530	-	-	1873
NF4	-	-	31	-	-	101	-	-	399
AQLM	69	-	-	81	-	-	312	-	-
QTIP	155	136	122	230	190	166	249	202	177
FLUTE	**173**	**150**	**139**	**687**	**592**	**548**	**2432**	**2122**	**1979**

Table 2: WikiText-2 PPL comparison of various 1-shot quantization methods for Llama-2-7b.

FP16		GPTQ	AQLM	QuIP#	QTIP	GPTQ+HIGGS ($p = 2$)
5.117	wbits≈2	-	8.180	8.220	6.820	8.637
	wbits≈3	5.776	-	5.600	5.380	5.559
	wbits≈4	5.254	-	5.220	5.170	5.213

fact to estimate these coefficients without using a real quantization method, and instead introduce a Gaussian noise insertion procedure, described in Appendix B.2. In this method we add normal noise to the weights that emulates the quantization error. An advantage that we get is that we can accuracy regulate t value. Then we apply multiple (J) calibration noise levels that are uniformly sampled from applicability region to each level to estimate the coefficients α_l. Algorithm 3 describes the procedure. Note that $W^\star(l, t_j)$ represents the model $W^\star$ with all layers intact except for layer l, which is replaced by $\widehat{W_l}$ via the Gaussian noise insertion procedure with noise t_j, described in Eqn. (9); see also (12). We found that sampling $J = 15$ noise levels from linear theorem applicability range is enough to get accurate coefficients α_l.

Measuring Grid Parameters. Grid bitwidths b_j are inherent grid parameters (e.g. supported bitwidths) and known by design. The grid distortions $t^2_{l,j}$ can be measured explicitly by quantizing $W^\star_l$ with $\mathcal{Q}_j$, creating a "database" of per-layer errors, across supported bitwidths.

Solving the Problem. We then solve the global minimization problem for the obtained α_l, b_j and t_{lj} coefficients, acquiring the optimal quantization configuration for the given average bitwidth. Since the error function to be minimized *is summable*, Equation 5 can be expressed as a linear programming problem, which can be solved using already existing optimization libraries. Specifically, we use the CP-SAT solver from Google OR-Tools library (Perron and Didier, 2024), that can optimally solve this problem. Figure 3 demonstrates the practical dependence of the optimized objective on budged $b_{\max}$.

Data Free Dynamic Quantization. We also present a data-free dynamic quantization mode for our method. Before, we used a calibration dataset to estimate the error coefficients α_l, making it data-dependent. To avoid the need for calibration dataset, we can change the metric we use in calibration described in Algorithm 3 from perplexity on a calibration dataset to KL-divergence between pretrained and quantized models on randomly sampled text tokens. We evaluate KL-divergence on 287k random tokens that are not shared between evaluations.

6 Experiments

6.1 Error Model Validation

One key point in the Theorem is that the result holds for *sufficiently small* relative per-layer quantization errors t_l. In this section, we seek to validate the fact that common bit-widths used in practice provide low enough compression error in order for the result to apply. We conduct experiments for data-free weight quantization of the popular Llama

Method	wbits	Wiki2	ArcC	ArcE	PiQA	Wino	HellaS	Avg	MMLU
FP16	16.00	5.607	51.28	81.52	80.03	73.72	60.01	69.31	65.35
AF	3.25	8.056	43.94	75.25	77.53	69.38	52.91	63.80	53.15
NF	3.25	7.683	42.66	75.63	77.97	70.48	54.92	64.33	55.82
HQQ	3.25	7.317	43.17	76.14	78.24	68.98	55.37	64.38	56.39
HIGGS (p=2)	3.25	7.110	44.11	76.35	77.09	73.09	55.77	65.28	57.56
HIGGS (p=3)	3.25	6.807	44.71	77.95	77.75	71.11	57.01	65.71	**60.11**
HIGGS (p=4)	3.25	**6.643**	47.27	78.41	78.45	70.72	56.97	**66.36**	59.88
GPTQ	3.25	7.133	41.13	72.81	75.14	71.51	53.86	62.89	58.37
HIGGS (dyn data-free)	3.25	**6.388**	47.10	79.12	78.78	71.59	57.09	**66.74**	**61.62**
AF	4.02	6.194	46.84	78.54	79.16	73.95	58.28	67.35	61.47
NF	4.02	6.225	47.95	79.38	79.27	73.24	58.44	67.66	62.65
HQQ	4.02	8.057	46.84	78.16	77.91	70.17	55.44	65.70	57.72
HIGGS (p=1)	4.02	6.142	47.27	79.63	78.78	72.45	58.29	67.28	61.74
HIGGS (p=2)	4.02	6.015	48.29	81.06	79.54	73.95	58.54	68.28	**63.26**
HIGGS (p=3)	4.02	**5.981**	50.17	80.26	80.30	73.72	59.17	**68.73**	62.83
GPTQ	4.02	6.238	45.82	78.66	78.02	72.53	56.91	66.39	62.96
HIGGS (dyn data-free)	4.00	**5.910**	49.23	80.98	79.38	72.85	59.00	**68.29**	**63.86**
AF	4.25	5.952	49.57	80.85	79.27	74.27	59.13	68.62	63.20
NF	4.25	5.964	49.32	80.81	78.94	73.40	59.16	68.33	64.10
HQQ	4.25	5.944	50.09	81.44	79.76	73.88	59.44	68.92	63.70
HIGGS (p=1)	4.26	5.978	50.26	80.98	79.54	73.24	58.96	68.60	63.47
HIGGS (p=2)	4.26	5.908	50.60	81.48	79.38	74.19	59.17	**68.96**	63.52
HIGGS (p=3)	4.25	**5.872**	49.57	81.27	79.38	72.38	59.33	68.39	**64.24**
GPTQ	4.25	5.923	47.18	79.59	79.16	72.22	58.43	67.32	64.06
HIGGS (dyn data-free)	4.25	**5.831**	50.43	81.27	79.43	72.85	59.33	**68.66**	**64.06**

Table 3: Quantized Llama3.1 8B perplexity on WikiText-2 (Merity et al., 2016b), accuracy on 5 zero-shot tasks (Gao et al., 2021), average zero-shot accuracy, and 5-shot accuracy on MMLU. All quantization methods are data-free. Experiment configurations are described in Appendix H.

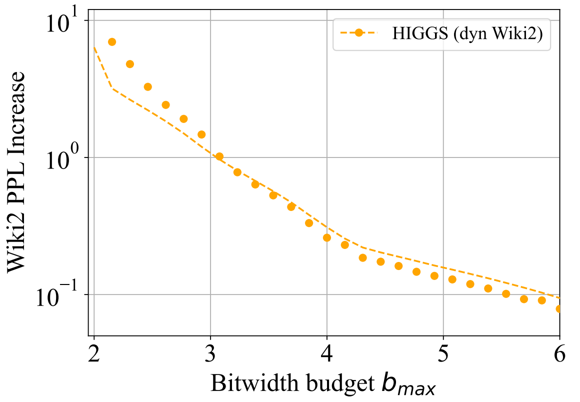

Figure 3: Demonstration of WikiText-2 PPL increase as a function of bitwidth budget $b_{\max}$ for layer-wise dynamic bitwidth quantization for Llama 3.1 8B. Dotted lines represent Linear Model predictions.

3.1 8B model with HIGGS quantization. To evaluate the error model, we compare the predicted perplexity with the real perplexity of the quantized model. For that, we uniformly quantize the model with different grid dimensions p and grid sizes n. We only use grids on pareto frontier of perplexity vs bitwidth with $1 \leq p \leq 5$ and $9 \leq n \leq 4096$.

Evaluated and predicted perplexities are shown in Figure 1. We observe that the predicted perplexity is close to the real perplexity on relatively higher bitwidths ($b > 3.0$) and diverges on lower bitwidths, where the quantization error is higher. Thus, we can use the error model in realistic bitwidth ranges.

6.2 Methods Evaluation

Methods. We compare HIGGS (Algorithm 2) with Normal Float (NF) (Dettmers et al., 2023a), Abnormal Float (AF) (Yoshida, 2023) and HQQ (Badri and Shaji, 2023). We provide detailed configurations and code sources for all the methods in Appendix H. One important thing to note is that constant bitwidth HIGGS configurations were chosen to be as close to the default bitwidths of other method as possible with no regard for availability of kernels to run them. Dynamic bitwidth HIGGS results, however, limited the configurations to those mentioned in Section 4.3: FLUTE grids and CH8.

Models. We compare the aforementioned methods in application to quantization of models from the Llama 3 Dubey et al. (2024) and Qwen2.5 (Bai et al., 2023) families of models. More specifically, we validate our findings on Llama3.2 1B (Table 7), Llama3.2 3B (Table 8), Llama3.1 8B (Table 3), Llama3.1 8B Instruct (Table 9), Llama3.1 70B (Table 10), and Qwen2.5 7B (Table 11).

Metrics. We report perplexity on WikiText-2 (Merity et al., 2016b) validation set. We measure zero-shot accuracy on WinoGrande (Sakaguchi et al., 2021), PiQA (Tata and Patel, 2003), HellaSwag (Zellers et al., 2019), ARC-easy and ARC-challenge (Clark et al., 2018), and report average zero-shot accuracy. We also report 5-shot accuracy on the MMLU (Hendrycks et al., 2021) benchmark. Zero-shot and few-shot measurements are done via the LM Eval Harness (Gao et al., 2021).

Table 4: Comparison with 1-shot quantization methods for Llama 3.1 8B quantization.

Method	wbits	Wiki2	MMLU
FP16	16	5.606	65.36
GPTQ	3.25	7.133	58.37
HIGGS (dyn data-free)	3.25	6.388	61.62
HIGGS (dyn)	3.25	6.359	61.37
GPTQ	4.02	6.238	62.96
AWQ	4.02	6.228	62.88
HIGGS (dyn data-free)	4.00	5.910	63.86
HIGGS (dyn)	4.00	5.870	63.69
GPTQ	4.25	5.923	64.05
AWQ	4.25	5.905	63.83
HIGGS (dyn data-free)	4.25	5.831	64.06
HIGGS (dyn)	4.25	5.802	64.26

Uniform Bitwidths. We present the Llama 3.1 8B evaluations in Table 3. Evaluations for other models are present in Appendix I. For bitwidths around or below 4.0, We can see that HIGGS outperforms all existing 0-shot compression methods even in the fixed-bitwidth applications.

Non-Uniform Bitwidths. We present the dynamic bitwidth results alongside the constant bitwidth results, in separate row groups in Tables 3, 7, 8, 9, 10, and 11. More specifically, we present results for data-free dynamic bitwidth quantization expansion of our method (dyn data-free), described in detail in Section 5. For calibration we use $J = 15$ noise values from linear theorem applicability range. We calibrate on 287k tokens from WikiText-2 (Merity et al., 2016b) train set.

Comparison With Data-Aware Methods. Additionally, we compare our data-free dynamic bitwidth HIGGS method with popular data-aware 1-shot quantization methods: GPTQ (Frantar et al., 2022) and AWQ (Lin et al., 2023). Alongside data-free method (dyn data-free), we present results for method calibrated on WikiText-2 PPL itself (dyn Wiki2). The results, shown in Table 4, indicate that HIGGS consistently outperforms those quantization methods as well. Moreover, we observe little difference in few-shot performance between data-free and data-dependent method.

7 Conclusions

We have presented a new result relating the per-layer quantization error with the model's global error, and have applied this result to two problems in LLM quantization: accurate data-free quantization and optimal non-uniform compression. Our approach leads to state-of-the-art performance for data-free quantization, and is compatible with efficient runtimes (Dettmers and von Koeller, 2021; Guo et al., 2024). Remarkably, we observe that our approach is robust to being made completely data-free via random sampling; moreover, it appears to outperform popular calibration-based methods in the 3-4 bits/parameter range.

8 Limitations

One direction for improvement is validating the approach across several model architecture types (e.g. Mixture-of-Experts). However, we believe our result should be generalizable, as the quantization approach used is model-independent. One other limitation is the requirement to use Hadamard transforms for weight incoherence, which may add runtime overheads in some cases. However, it is known (Chee et al., 2023) that these runtimes can be minimized, or that the corresponding matrices can even be eliminated by "folding them into" the previous layer (Ashkboos et al., 2024). We aim to investigate this in future work, as further enhancements to existing kernels such as FLUTE (Guo et al., 2024).

References

Nir Ailon and Bernard Chazelle. 2009. The fast johnson–lindenstrauss transform and approximate nearest neighbors. *SIAM Journal on Computing*, 39(1):302–322.

Saleh Ashkboos, Amirkeivan Mohtashami, Maximilian L. Croci, Bo Li, Martin Jaggi, Dan Alistarh, Torsten Hoefler, and James Hensman. 2024. Quarot: Outlier-free 4-bit inference in rotated llms. *Preprint*, arXiv:2404.00456.

Hicham Badri and Appu Shaji. 2023. Half-quadratic quantization of large machine learning models.

Jinze Bai, Shuai Bai, Yunfei Chu, Zeyu Cui, Kai Dang, Xiaodong Deng, Yang Fan, Wenbin Ge, Yu Han, Fei Huang, et al. 2023. Qwen technical report. *arXiv preprint arXiv:2309.16609*.

Jerry Chee, Yaohui Cai, Volodymyr Kuleshov, and Christopher De Sa. 2023. Quip: 2-bit quantization of large language models with guarantees. *Preprint*, arXiv:2307.13304.

Peter Clark, Isaac Cowhey, Oren Etzioni, Tushar Khot, Ashish Sabharwal, Carissa Schoenick, and Oyvind Tafjord. 2018. Think you have solved question answering? try arc, the ai2 reasoning challenge. *arXiv preprint arXiv:1803.05457*.

Peter Davies, Vijaykrishna Gurunathan, Niusha Moshrefi, Saleh Ashkboos, and Dan Alistarh. 2020. New bounds for distributed mean estimation and variance reduction. *arXiv preprint arXiv:2002.09268*.

Tim Dettmers, Mike Lewis, Younes Belkada, and Luke Zettlemoyer. 2022. LLM.int8(): 8-bit matrix multiplication for transformers at scale. *Advances in Neural Information Processing Systems 35: Annual Conference on Neural Information Processing Systems 2022, NeurIPS 2022*.

Tim Dettmers, Artidoro Pagnoni, Ari Holtzman, and Luke Zettlemoyer. 2023a. Qlora: Efficient finetuning of quantized llms. *Preprint*, arXiv:2305.14314.

Tim Dettmers, Ruslan Svirschevski, Vage Egiazarian, Denis Kuznedelev, Elias Frantar, Saleh Ashkboos, Alexander Borzunov, Torsten Hoefler, and Dan Alistarh. 2023b. SpQR: A sparse-quantized representation for near-lossless llm weight compression. *arXiv preprint arXiv:2306.03078*.

Tim Dettmers and Titus von Koeller. 2021. Accessible large language models via k-bit quantization for pytorch.

Tim Dettmers and Luke Zettlemoyer. 2022. The case for 4-bit precision: k-bit inference scaling laws. *arXiv preprint arXiv:2212.09720*.

Abhimanyu Dubey, Abhinav Jauhri, Abhinav Pandey, Abhishek Kadian, and et al. 2024. The Llama 3 herd of models. *Preprint*, arXiv:2407.21783.

Vage Egiazarian, Andrei Panferov, Denis Kuznedelev, Elias Frantar, Artem Babenko, and Dan Alistarh. 2024. Extreme compression of large language models via additive quantization. *arXiv preprint arXiv:2401.06118*.

Elias Frantar and Dan Alistarh. 2022. SPDY: Accurate pruning with speedup guarantees. *arXiv preprint arXiv:2201.13096*.

Elias Frantar, Saleh Ashkboos, Torsten Hoefler, and Dan Alistarh. 2022. Gptq: Accurate post-training quantization for generative pre-trained transformers. *arXiv preprint arXiv:2210.17323*.

Elias Frantar, Roberto L. Castro, Jiale Chen, Torsten Hoefler, and Dan Alistarh. 2024. Marlin: Mixed-precision auto-regressive parallel inference on large language models. *Preprint*, arXiv:2408.11743.

Leo Gao, Jonathan Tow, Stella Biderman, Sid Black, Anthony DiPofi, Charles Foster, Laurence Golding, Jeffrey Hsu, Kyle McDonell, Niklas Muennighoff, Jason Phang, Laria Reynolds, Eric Tang, Anish Thite, Ben Wang, Kevin Wang, and Andy Zou. 2021. A framework for few-shot language model evaluation.

Amir Gholami, Sehoon Kim, Zhen Dong, Zhewei Yao, Michael W Mahoney, and Kurt Keutzer. 2021. A survey of quantization methods for efficient neural network inference. *arXiv preprint arXiv:2103.13630*.

Han Guo, William Brandon, Radostin Cholakov, Jonathan Ragan-Kelley, Eric P. Xing, and Yoon Kim. 2024. Fast matrix multiplications for lookup table-quantized llms. *Preprint*, arXiv:2407.10960.

Dan Hendrycks, Collin Burns, Steven Basart, Andy Zou, Mantas Mazeika, Dawn Song, and Jacob Steinhardt. 2021. Measuring massive multitask language understanding. *Preprint*, arXiv:2009.03300.

Sehoon Kim, Coleman Hooper, Amir Gholami, Zhen Dong, Xiuyu Li, Sheng Shen, Michael W Mahoney, and Kurt Keutzer. 2023. Squeezellm: Dense-and-sparse quantization. *arXiv preprint arXiv:2306.07629*.

Woosuk Kwon, Zhuohan Li, Siyuan Zhuang, Ying Sheng, Lianmin Zheng, Cody Hao Yu, Joseph E. Gonzalez, Hao Zhang, and Ion Stoica. 2023. Efficient memory management for large language model serving with pagedattention. In *Proceedings of the ACM SIGOPS 29th Symposium on Operating Systems Principles*.

Changhun Lee, Jungyu Jin, Taesu Kim, Hyungjun Kim, and Eunhyeok Park. 2024. Owq: Outlier-aware weight quantization for efficient fine-tuning and inference of large language models. *Preprint*, arXiv:2306.02272.

Ji Lin, Jiaming Tang, Haotian Tang, Shang Yang, Xingyu Dang, and Song Han. 2023. Awq: Activation-aware weight quantization for llm compression and acceleration. *arXiv preprint arXiv:2306.00978*.

Zechun Liu, Changsheng Zhao, Igor Fedorov, Bilge Soran, Dhruv Choudhary, Raghuraman Krishnamoorthi, Vikas Chandra, Yuandong Tian, and Tijmen Blankevoort. 2024. Spinquant: Llm quantization with learned rotations. *Preprint*, arXiv:2405.16406.

Stephen Merity, Caiming Xiong, James Bradbury, and Richard Socher. 2016a. Pointer sentinel mixture models. *Preprint*, arXiv:1609.07843.

Stephen Merity, Caiming Xiong, James Bradbury, and Richard Socher. 2016b. Pointer sentinel mixture models. *arXiv preprint arXiv:1609.07843*.

Markus Nagel, Rana Ali Amjad, Mart Van Baalen, Christos Louizos, and Tijmen Blankevoort. 2020. Up or down? Adaptive rounding for post-training quantization. In *International Conference on Machine Learning (ICML)*.

Gilles Pagès and Jacques Printems. 2003. Optimal quadratic quantization for numerics: the gaussian case. *Monte Carlo Methods and Applications*, 9:135–166.

Gunho Park, Baeseong Park, Se Jung Kwon, Byeongwook Kim, Youngjoo Lee, and Dongsoo Lee. 2022. nuQmm: Quantized matmul for efficient inference of large-scale generative language models. *arXiv preprint arXiv:2206.09557*.

Adam Paszke, Sam Gross, Francisco Massa, Adam Lerer, James Bradbury, Gregory Chanan, Trevor Killeen, Zeming Lin, Natalia Gimelshein, Luca Antiga, et al. 2019. Pytorch: An imperative style, high-performance deep learning library. *Advances in neural information processing systems*, 32.

Laurent Perron and Frédéric Didier. 2024. Cp-sat.

Keisuke Sakaguchi, Ronan Le Bras, Chandra Bhagavatula, and Yejin Choi. 2021. Winogrande: an adversarial winograd schema challenge at scale. *Commun. ACM*, 64(9):99–106.

Ananda Theertha Suresh, Felix X. Yu, Sanjiv Kumar, and H. Brendan McMahan. 2017. Distributed mean estimation with limited communication. *Preprint*, arXiv:1611.00429.

Sandeep Tata and Jignesh M Patel. 2003. PiQA: An algebra for querying protein data sets. In *International Conference on Scientific and Statistical Database Management*.

torchao maintainers and contributors. 2024. torchao: Pytorch native quantization and sparsity for training and inference.

Albert Tseng, Jerry Chee, Qingyao Sun, Volodymyr Kuleshov, and Christopher De Sa. 2024a. Quip#: Even better llm quantization with hadamard incoherence and lattice codebooks. *Preprint*, arXiv:2402.04396.

Albert Tseng, Qingyao Sun, David Hou, and Christopher De Sa. 2024b. Qtip: Quantization with trellises and incoherence processing. *arXiv preprint arXiv:2406.11235*.

Mart van Baalen, Andrey Kuzmin, Markus Nagel, Peter Couperus, Cedric Bastoul, Eric Mahurin, Tijmen Blankevoort, and Paul Whatmough. 2024. Gptvq: The blessing of dimensionality for llm quantization. *arXiv preprint arXiv:2402.15319*.

Shay Vargaftik, Ran Ben Basat, Amit Portnoy, Gal Mendelson, Yaniv Ben-Itzhak, and Michael Mitzenmacher. 2021. Drive: One-bit distributed mean estimation. *Preprint*, arXiv:2105.08339.

Shay Vargaftik, Ran Ben Basat, Amit Portnoy, Gal Mendelson, Yaniv Ben-Itzhak, and Michael Mitzenmacher. 2022. Eden: Communication-efficient and robust distributed mean estimation for federated learning. *Preprint*, arXiv:2108.08842.

Lei Wang, Lingxiao Ma, Shijie Cao, Quanlu Zhang, Jilong Xue, Yining Shi, Ningxin Zheng, Ziming Miao, Fan Yang, Ting Cao, Yuqing Yang, and Mao Yang. 2024. Ladder: Enabling efficient low-precision deep learning computing through hardware-aware tensor transformation. In *18th USENIX Symposium on Operating Systems Design and Implementation (OSDI 24)*, pages 307–323, Santa Clara, CA. USENIX Association.

Haojun Xia, Zhen Zheng, Xiaoxia Wu, Shiyang Chen, Zhewei Yao, Stephen Youn, Arash Bakhtiari, Michael Wyatt, Donglin Zhuang, Zhongzhu Zhou, et al. 2024. Fp6-llm: Efficiently serving large language models through fp6-centric algorithm-system co-design. *arXiv preprint arXiv:2401.14112*.

Zhewei Yao, Reza Yazdani Aminabadi, Minjia Zhang, Xiaoxia Wu, Conglong Li, and Yuxiong He. 2022. Zeroquant: Efficient and affordable post-training quantization for large-scale transformers. *arXiv preprint arXiv:2206.01861*.

Lu Yin, You Wu, Zhenyu Zhang, Cheng-Yu Hsieh, Yaqing Wang, Yiling Jia, Gen Li, Ajay Jaiswal, Mykola Pechenizkiy, Yi Liang, Michael Bendersky, Zhangyang Wang, and Shiwei Liu. 2024. Outlier weighed layerwise sparsity (owl): A missing secret sauce for pruning llms to high sparsity. *Preprint*, arXiv:2310.05175.

Davis Yoshida. 2023. Nf4 isn't information theoretically optimal (and that's good). *Preprint*, arXiv:2306.06965.

Rowan Zellers, Ari Holtzman, Yonatan Bisk, Ali Farhadi, and Yejin Choi. 2019. Hellaswag: Can a machine really finish your sentence? In *Proceedings of the 57th Conference of the Association for Computational Linguistics, ACL 2019, Florence, Italy, July 28- August 2, 2019, Volume 1: Long Papers*, pages 4791–4800. Association for Computational Linguistics.

Susan Zhang, Stephen Roller, Naman Goyal, Mikel Artetxe, Moya Chen, Shuohui Chen, Christopher Dewan, Mona Diab, Xian Li, Xi Victoria Lin, et al. 2022. Opt: Open pre-trained transformer language models. *arXiv preprint arXiv:2205.01068*.

A Table of Notation

Notation	Meaning	Reference
L	number of matrices the entries of which we want to quantize	
W_l	matrix of floats corresponding to layer $l \in \{1, \ldots, L\}$	
$d_{in}^l \times d_{out}^l$	dimensions of matrix W_l	
d_l	$= d_{in}^l \cdot d_{out}^l$	
$\mathcal{C}_l$	a (possibly randomized) compression mapping used to compress W_l	
$\mathcal{G}_l$	Gaussian noise insertion (a special type of compressor $\mathcal{C}_l$)	(9)
$\widehat{W_l}$	$= \mathcal{C}_l(W_l)$; compressed version of matrix W_l	
W	$= (W_1, \ldots, W_L)$	
$W^\star$	$= (W_1^\star, \ldots, W_L^\star)$; weights of a pre-trained model	
$PPL(W)$	the perplexity of the model associated with weights W	
d	$= \sum_{l=1}^L d_{in}^l \cdot d_{out}^l$; the total number of floats in the model we want to quantize	
$\mathcal{G}_n^p$	a grid: a collection of n vectors in $\mathbb{R}^p$ used for quantization by rounding to the nearest	

Table 5: Selected frequently used notation.

B Compression of Linear Layers

B.1 Compressing linear layers

Let $\mathcal{C}_l : \mathbb{R}^{d_{in}^l \times d_{out}^l} \to \mathbb{R}^{d_{in}^l \times d_{out}^l}$ be a (possibly randomized) compression (e.g., sparsification and/or quantization) mechanism and let $\widehat{W_l} := \mathcal{C}_l(W_l) \in \mathbb{R}^{d_{in}^l \times d_{out}^l}$ represent a compressed/quantized version of W_l. Further, let

$$t_l^2 = t_l^2(W_l, \mathcal{C}_l) := \frac{\mathrm{E}\left[\|\mathcal{C}_l(W_l) - W_l\|_F^2\right]}{\|W_l\|_F^2}, \quad l = 1, \ldots, L. \tag{6}$$

That is,

$$\mathrm{E}\left[\|\widehat{W_l} - W_l\|_F^2\right] = t_l^2(W_l, \mathcal{C}_l)\|W_l\|_F^2, \quad l = 1, \ldots, L. \tag{7}$$

Here we remark that the highly studied class of *contractive* compressors is characterized by the inequality

$$\mathrm{E}\left[\|\mathcal{C}_l(W_l) - W_l\|_F^2\right] \leq (1 - \alpha_l)\|W_l\|_F^2, \quad \forall W_l \in \mathbb{R}^{d_{in}^l \times d_{out}^l}, \quad \forall l \in \{1, \ldots, L\}, \tag{8}$$

which is assumed to hold for some $0 < \alpha_l \leq 1$. If we apply such a contractive compressor to W_l, we get

$$t_l^2(W_l, \mathcal{C}_l)\|W_l\|_F^2 \overset{Equation\ (7)}{=} \mathrm{E}\left[\|\mathcal{C}_l(W_l) - W_l\|_F^2\right] \overset{Equation\ (8)}{\leq} (1 - \alpha_l)\|W_l\|_F^2,$$

which means that

$$t_l^2(W_l, \mathcal{C}_l) \leq 1 - \alpha_t.$$

In other words, unlike the contraction factor $1 - \alpha_t$, which needs to hold universally for all matrices $W_l \in \mathbb{R}^{d_{in}^l \times d_{out}^l}$, $t_l^2(W_l, \mathcal{C}_l)$ is an "instantaneous" contraction factor corresponding to W_l only, and as such, is always not worse, and typically much better.

B.2 Gaussian noise insertion

We now describe a synthetic noise insertion procedure whose role is to mimic the error due to compression. Given a constant $t > 0$, define

$$\mathcal{G}_l(W_l, t) := W_l + \frac{t\|W_l\|_F}{\sqrt{d_{in}^l \cdot d_{out}^l}} \Sigma_l, \quad l = 1, \ldots, L, \tag{9}$$

where the entries of $\Sigma_l \in \mathbb{R}^{d_{in}^l \times d_{out}^l}$ are all i.i.d. Gaussians with zero mean and unit variance. This means that the entries of $\mathcal{G}_l(W_l, t)$ are also Gaussians, with mean determined by the entries of W_l, and variance $\sigma_l^2 := t^2\|W_l\|_F^2$. This implies that

$$\mathrm{E}\left[\|\mathcal{G}_l(W_l, t) - W_l\|_F^2\right] = t^2\|W_l\|_F^2, \quad l = 1, \ldots, L. \tag{10}$$

Comparing this to (7), we see that

$$t_l^2(W_l, \mathcal{G}_l(\cdot, t)) = t^2.$$

C Empirical Approximation of Perplexity Around the Pre-trained Model

Let $PPL(W)$ denote the perplexity of the model corresponding to weights W, and let $W^\star$ be the weights corresponding to a pre-trained model. We have made the following (perhaps surprising!) observation through numerical experimentation: if we replace the pre-trained weights $W_l^\star$ of the l^{th} layer by $\widehat{W}_l = \mathcal{C}_l(W_l^\star)$, where $\mathcal{C}_l$ is a contractive compressor, then

$$PPL(W_1^\star, \ldots, W_{l-1}^\star, \widehat{W}_l, W_{l+1}^\star, \ldots, W_L^\star) \approx PPL(W^\star) + \alpha_l t_l^2 \tag{11}$$

for all $t_l \in [0, \bar{t}_l]$, where $\bar{t}_l$ is "small enough"[1], and for some coefficient $\alpha_l > 0$ computed via linear regression. If we specialize

$$\widehat{W}_l = \mathcal{C}_l(W_l^\star) := \mathcal{G}_l(W_l^\star, t),$$

then the model $W^\star(l,t)$ described in Section 5 and Algorithm 3 is defined as

$$W^\star(l,t) := (W_1^\star, \ldots, W_{l-1}^\star, \mathcal{G}_l(W_l^\star, t), W_{l+1}^\star, \ldots, W_L^\star). \tag{12}$$

Moreover, a stronger experimental observation was made: if we replace the pre-trained weights of *all layers* by $\widehat{W}_l = \mathcal{C}_l(W_l^\star)$, where $\mathcal{C}_l$ is a contractive compressor, then

$$PPL(\widehat{W}) \approx PPL(W^\star) + \sum_{l=1}^{L} \alpha_l t_l^2 \tag{13}$$

for $t_l \in [0, \bar{t}_l]$, where $\bar{t}_l$ is "small enough", and for some coefficient $\alpha_l > 0$ computed via linear regression.

This latter observation is formalized as Theorem 1, and proved in the next section.

D Theoretical Approximation of Perplexity Around the Pre-trained Model

D.1 Proof of Theorem 1

Proof. The proof follows from the material included in Section D.4. The material in Sections D.2 and D.3 provides a simplified treatment, and is included for clarity/pedagogical reasons. □

D.2 Approximating the mean of a smooth function perturbed around a local minimizer: univariate case

Consider a sufficiently smooth function $\phi : \mathbb{R} \to \mathbb{R}$. Let $w^\star \in \mathbb{R}$ be a local minimizer of ϕ, whence $\phi'(w^\star) = 0$. Let ξ be any random variable with finite second moment:

$$M_2 := \mathrm{E}\left[\xi^2\right] < +\infty.$$

From Taylor's approximation of ϕ around $w^\star$, we get

$$\begin{aligned}\phi(w^\star + t|w^\star|\xi) &\approx \phi(w^\star) + \phi'(w^\star)t|w^\star|\xi + \frac{1}{2}\phi''(w^\star)t^2|w^\star|^2\xi^2 \\ &= \phi(w^\star) + \frac{1}{2}\phi''(w^\star)t^2|w^\star|^2\xi^2.\end{aligned}$$

Taking expectation on both sides, we get

$$\begin{aligned}\mathrm{E}\left[\phi(w^\star + t|w^\star|\xi)\right] &\approx \mathrm{E}\left[\phi(w^\star) + \frac{1}{2}\phi''(w^\star)t^2|w^\star|^2\xi^2\right] \\ &= \phi(w^\star) + \frac{1}{2}\phi''(w^\star)t^2|w^\star|^2\mathrm{E}\left[\xi^2\right] \\ &= \phi(w^\star) + \frac{1}{2}\phi''(w^\star)t^2|w^\star|^2 \\ &= \phi(w^\star) + \alpha t^2 M_2,\end{aligned}$$

where $\alpha := \frac{1}{2}\phi''(w^\star)|w^\star|^2 M_2$.

Let us now make above approximation more precise. In order to do so, we will rely on two additional assumptions:

[1] Add some comment on how small it is.

(i) the third derivative of ϕ is bounded by $B_3 > 0$: $|\phi'''(t)| \leq B_3$ for all $t \in \mathbb{R}$;

(ii) the third moment of $|\xi|$ is finite: $M_3 := \mathrm{E}\left[|\xi|^3\right] < +\infty$.

Under these assumptions, there exists θ_ξ on the interval defined by $w^\star$ and $w^\star + t|w^\star|\xi$ such that

$$\begin{aligned}\phi(w^\star + t|w^\star|\xi) &= \phi(w^\star) + \phi'(w^\star)t|w^\star|\xi + \frac{1}{2}\phi''(w^\star)t^2|w^\star|^2\xi^2 + \frac{1}{6}\phi'''(\theta_\xi)t^3|w^\star|^3\xi^3 \\ &= \phi(w^\star) + \frac{1}{2}\phi''(w^\star)t^2|w^\star|^2\xi^2 + \frac{1}{6}\phi'''(\theta_\xi)t^3|w^\star|^3\xi^3.\end{aligned}$$

By taking expectation on both sides, we get

$$\mathrm{E}\left[\phi(w^\star + t|w^\star|\xi)\right] = \phi(w^\star) + \frac{1}{2}\phi''(w^\star)t^2|w^\star|^2 M_2 + \mathrm{E}\left[\frac{1}{6}\phi'''(\theta_\xi)t^3|w^\star|^3\xi^3\right],$$

from which we get the estimate

$$\begin{aligned}\left|\mathrm{E}\left[\phi(w^\star + t|w^\star|\xi)\right] - \left(\phi(w^\star) + \frac{1}{2}\phi''(w^\star)t^2|w^\star|^2 M_2\right)\right| &\leq \left|\mathrm{E}\left[\frac{1}{6}\phi'''(\theta_\xi)t^3|w^\star|^3\xi^3\right]\right| \\ &\leq \mathrm{E}\left[\left|\frac{1}{6}\phi'''(\theta_\xi)t^3|w^\star|^3\xi^3\right|\right] \\ &= \frac{1}{6}|t|^3|w^\star|^3\mathrm{E}\left[|\phi'''(\theta_\xi)|\,|\xi|^3\right] \\ &\leq \frac{1}{6}|t|^3|w^\star|^3 B_3 M_3.\end{aligned}$$

D.3 Approximating the mean of a smooth function perturbed around a local minimizer: multivariate case

Let's now consider the multivariate case. Consider a sufficiently smooth function $\phi : \mathbb{R}^d \to \mathbb{R}$. Let $\mathbf{w}^\star \in \mathbb{R}^d$ be a local minimizer of ϕ, whence $\nabla\phi(\mathbf{w}^\star) = 0$. Let $\xi = (\xi_1, \ldots, \xi_d)$ be a random vector such that the second moment

$$M_{2,i} := \mathrm{E}\left[\xi_i^2\right]$$

is finite for all $i \in \{1, \ldots, d\}$. Let $T = \mathit{Diag}(t_1, \ldots, t_d)$ and $D = \mathit{Diag}(|\mathbf{w}_1^\star|, \ldots, |\mathbf{w}_d^\star|)$, where $t_1, \ldots, t_d > 0$. From Taylor's approximation of ϕ around $\mathbf{w}^\star$, we get

$$\begin{aligned}\phi(\mathbf{w}^\star + DT\xi) &\approx \phi(\mathbf{w}^\star) + \langle\nabla\phi(\mathbf{w}^\star), DT\xi\rangle + \frac{1}{2}\left\langle\nabla^2\phi(\mathbf{w}^\star)DT\xi, DT\xi\right\rangle \\ &= \phi(\mathbf{w}^\star) + \frac{1}{2}\left\langle\nabla^2\phi(\mathbf{w}^\star)DT\xi, DT\xi\right\rangle \\ &= \phi(\mathbf{w}^\star) + \frac{1}{2}\left\langle D\nabla^2\phi(\mathbf{w}^\star)DT\xi, T\xi\right\rangle.\end{aligned}$$

Let's assume that $D\nabla^2\phi(\mathbf{w}^\star)D$ is approximately diagonal, i.e., there exists a diagonal matrix $Z = \mathit{Diag}(z_1, \ldots, z_d)$ with $z_l > 0$ for all l such that $D\nabla^2\phi(\mathbf{w}^\star)D \approx Z$. Under this assumption,

$$\left\langle D\nabla^2\phi(\mathbf{w}^\star)DT\xi, T\xi\right\rangle \approx \langle ZT\xi, T\xi\rangle = \sum_{i=1}^{d} z_i t_i^2 \xi_i^2, \tag{14}$$

and hence

$$\begin{aligned}
\mathrm{E}\left[\phi(\mathbf{w}^\star + DT\xi)\right] &\approx \mathrm{E}\left[\phi(\mathbf{w}^\star) + \frac{1}{2}\langle ZT\xi, T\xi\rangle\right] \\
&= \phi(\mathbf{w}^\star) + \frac{1}{2}\mathrm{E}\left[\langle ZT\xi, T\xi\rangle\right] \\
&\overset{Equation\ (14)}{=} \phi(\mathbf{w}^\star) + \frac{1}{2}\mathrm{E}\left[\sum_{i=1}^{d} z_i t_i^2 \xi_i^2\right] \\
&= \phi(\mathbf{w}^\star) + \frac{1}{2}\sum_{i=1}^{d} z_i t_i^2 \mathrm{E}\left[\xi_i^2\right] \\
&= \phi(\mathbf{w}^\star) + \frac{1}{2}\sum_{i=1}^{d} z_i t_i^2 M_{2,i} \\
&= \phi(\mathbf{w}^\star) + \sum_{i=1}^{d} \alpha_i t_i^2,
\end{aligned}$$

where $\alpha_i := \frac{z_i M_{2,i}}{2}$.

D.4 Approximating the mean of a smooth function perturbed around a local minimizer: multivariate block case

Let's now extend the last result to the multivariate *block* setting. Consider a sufficiently smooth function $\phi : \mathbb{R}^d \to \mathbb{R}$, where $d = d_1 + \cdots + d_L$. For $\mathbf{w} \in \mathbb{R}^d$ we shall write $\mathbf{w} = (\mathbf{w}_1, \ldots, \mathbf{w}_L)$, where $\mathbf{w}_l \in \mathbb{R}^{d_l}$ is the l^{th} block of vector $\mathbf{w}$. Let $\mathbf{w}^\star = (\mathbf{w}^{\star,1}, \ldots \mathbf{w}^{\star,L}) \in \mathbb{R}^d$ be a local minimizer of ϕ, whence

$$\nabla\phi(\mathbf{w}^\star) = 0. \tag{15}$$

Let $\xi = (\xi_1, \ldots, \xi_L)$ be a random vector in $\mathbb{R}^d$ such that the block $\xi_l \in \mathbb{R}^{d_l}$ has finite second moment:

$$M_{2,l} := \mathrm{E}\left[\|\xi_l\|_2^2\right] \tag{16}$$

for all $l \in \{1, \ldots, L\}$.

For each $l \in \{1, \ldots, L\}$, let $T_l := t_l I_{d_l} \in \mathbb{R}^{d_l \times d_l}$ and $D_l := \|\mathbf{w}^{\star,l}\|_2 I_{d_l} \in \mathbb{R}^{d_l \times d_l}$. Further, let $T := Diag(T_1, \ldots, T_L) \in \mathbb{R}^{d \times d}$ and $D := Diag(D_1, \ldots, D_L) \in \mathbb{R}^{d \times d}$. That is, D (resp. T) be the blog-diagonal matrix whose blocks are formed from the matrices $\{D_l\}$ (resp. $\{T_l\}$). From Taylor's approximation of ϕ around $\mathbf{w}^\star$, we get

$$\begin{aligned}
\phi(\mathbf{w}^\star + DT\xi) &\approx \phi(\mathbf{w}^\star) + \langle\nabla\phi(\mathbf{w}^\star), DT\xi\rangle + \frac{1}{2}\left\langle\nabla^2\phi(\mathbf{w}^\star)DT\xi, DT\xi\right\rangle \\
&\overset{Equation\ (15)}{=} \phi(\mathbf{w}^\star) + \frac{1}{2}\left\langle\nabla^2\phi(\mathbf{w}^\star)DT\xi, DT\xi\right\rangle \\
&= \phi(\mathbf{w}^\star) + \frac{1}{2}\left\langle D\nabla^2\phi(\mathbf{w}^\star)DT\xi, T\xi\right\rangle.
\end{aligned}$$

Let's assume that $D\nabla^2\phi(\mathbf{w}^\star)D$ is approximately block-diagonal, i.e., there exists a block-diagonal matrix $Z = Diag(Z_1, \ldots, Z_L)$ such that $D\nabla^2\phi(\mathbf{w}^\star)D \approx Z$. Moreover, assume that $Z_l = z_l I_{d_l}$ for some $z_l > 0$ and all $l \in \{1, \ldots, L\}$. Under this assumption,

$$\left\langle D\nabla^2\phi(\mathbf{w}^\star)DT\xi, T\xi\right\rangle \approx \langle ZT\xi, T\xi\rangle = \sum_{l=1}^{L}\langle Z_l T_l \xi_l, T_l \xi_l\rangle = \sum_{l=1}^{L} t_l^2 z_l \|\xi_l\|_2^2, \tag{17}$$

and hence

$$
\begin{aligned}
\mathrm{E}\left[\phi(\mathbf{w}^\star + DT\xi)\right] \quad &\approx \quad \mathrm{E}\left[\phi(\mathbf{w}^\star) + \frac{1}{2}\left\langle ZT\xi, T\xi\right\rangle\right] \\
&= \quad \phi(\mathbf{w}^\star) + \frac{1}{2}\mathrm{E}\left[\left\langle ZT\xi, T\xi\right\rangle\right] \\
&\overset{Equation\ (17)}{=} \quad \phi(\mathbf{w}^\star) + \frac{1}{2}\mathrm{E}\left[\sum_{l=1}^{L} t_l^2 z_l \|\xi_l\|_2^2\right] \\
&= \quad \phi(\mathbf{w}^\star) + \frac{1}{2}\sum_{l=1}^{L} t_l^2 z_l \mathrm{E}\left[\|\xi_l\|_2^2\right] \\
&\overset{Equation\ (16)}{=} \quad \phi(\mathbf{w}^\star) + \frac{1}{2}\sum_{l=1}^{L} t_l^2 z_l M_{2,l} \\
&= \quad \phi(\mathbf{w}^\star) + \sum_{l=1}^{L} \alpha_l t_l^2,
\end{aligned}
$$

where $\alpha_l := \frac{z_l M_{2,l}}{2}$.

E Experimental Justification of Assumption 3

In this section we justify Assumption 3 by analyzing the Hessian of the OPT-125M model (Zhang et al., 2022). This model consists of 12 blocks, each containing multiple matrices. Computing the full Hessian for even a single matrix from the self attention of the first layer is infeasible due to its size – $768 \times 768 = 589{,}824$ parameters, leading to a Hessian with around 400 Billion entries.

Given these constraints, we focused on a smaller scope of $t \in \mathbb{N}$ parameters of the module from every layer. Figure 4 illustrates the structure of the product in Equation (2).

We can see a clear diagonal structure of the product $D^\star \nabla^2 \phi\left(\mathcal{R}(W^\star)\right) D^\star$. We observed the same diagonal structure under several other parameter samples for OPT-125M for the product $D^\star \nabla^2 \phi\left(\mathcal{R}(W^\star)\right) D^\star$ in Assumption 3. Hence, this suggests that Assumption 3 is satisfied.

E.1 Experimental setup

To justify the Assumption 3 we have made various experiments with a OPT-125M model (Zhang et al., 2022). The OPT-125M model consists of $B = 12$ subsequent blocks, each containing multiple layers (matrices). For every block $i \in \{1, \cdots, B\}$ we have the following linear layers:

- Self attention:
  - q_proj: $Q_i \in \mathbb{R}^{768\times768}$
  - v_proj: $V_i \in \mathbb{R}^{768\times768}$
  - k_proj: $K_i \in \mathbb{R}^{768\times768}$
  - out_proj: $O_i \in \mathbb{R}^{768\times768}$
- First fully connected layer: $C_i \in \mathbb{R}^{768\times3072}$
- Second fully connected layer: $S_i \in \mathbb{R}^{3072\times768}$

Let us define $m \in \mathbb{N}$ – the number of layers in a blocks. For OPT-125M, $m = 6$. Since we have $B = 12$ blocks with $m = 6$ layers in each, in total there are $L = Bm = 72$ layers, so $l \in \{1, \cdots, 72\}$.

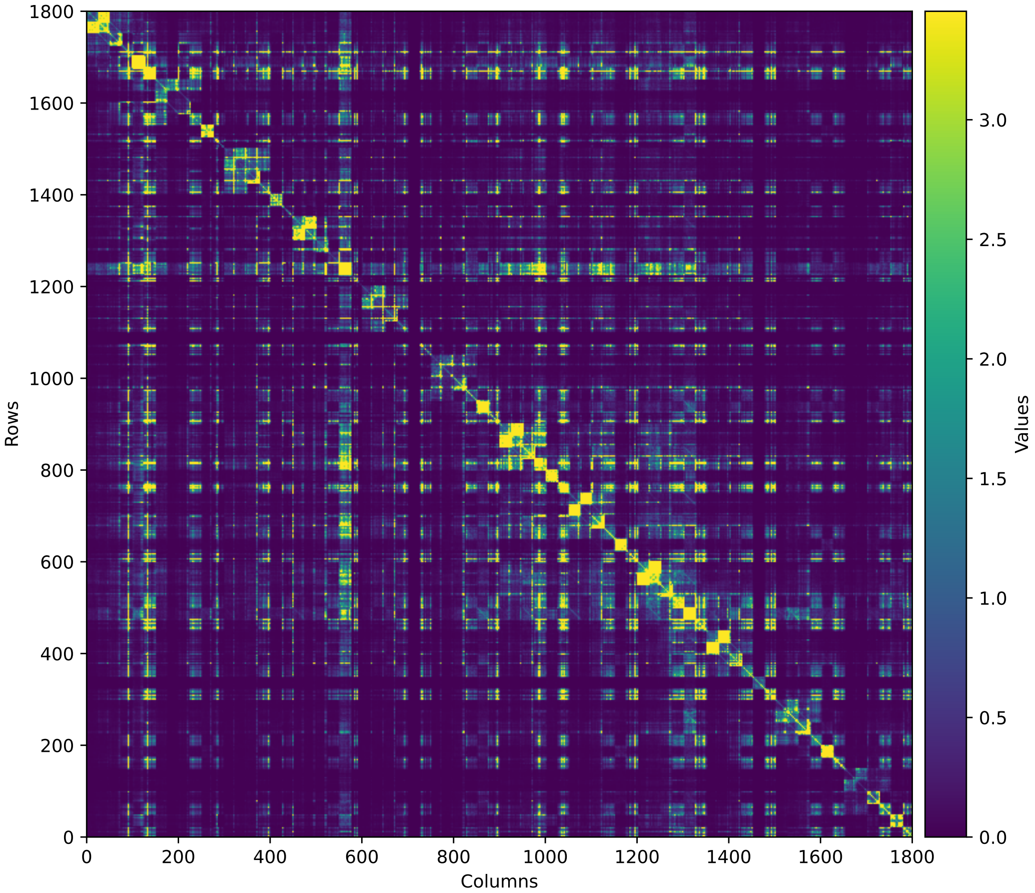

Figure 4: Visual representation of part of the product $|D^{\star}\nabla^2\phi\left(\mathcal{R}(W^{\star})\right)D^{\star}|$. The diagonal-dominant structure justifies the Assumption 3. Please see Appendix Figure 5) for additional subsets.

E.2 Single layer from a single block

Computing the full Hessian $\nabla^2\phi\left(\mathcal{R}(Q_1)\right)$ for even a single $Q_1 \in \mathbb{R}^{768\times 768}$ matrix from a self attention of the first block is infeasible due to its size – 768×768 results in $589,824$ parameters, leading to a Hessian with around 400 billion elements.

Given these constraints, we decided to focus on a smaller scope of $t \in \mathbb{N}$ parameters of the module. Let us consider some layer $W_l \in \mathbb{R}^{d^l_{in}\times d^l_{out}}$.

In this section we will use the following notation for entries of vectors and matrices: for any vector r, we denote $[r]_i$ as the i-th element of the vector r. Similarly, for any matrix A, we denote $[A]_{ij}$ as the element of A in the intersection of the i-th row and j-th column.

Now let us consider the first $t \in \{1, \cdots, d^l_{in}\cdot d^l_{out}\}$ entries of the matrix W_l – the vector $\widetilde{W_l} = [\mathcal{R}(W_l)]_{:t}$, $\widetilde{W_l} \in \mathbb{R}^t$. With these notation we define a concatenation function $\psi_{W_l} : \mathbb{R}^t \to \mathbb{R}^{d^l_{in}\cdot d^l_{out}}$:

$$\psi_{W_l}(\widetilde{W_l}) = \left(\widetilde{W_l}, [\mathcal{R}(W_l)]_{t:}\right).$$

Finally, let us define the perplexity function $\widetilde{\phi}_{W_l} : \mathbb{R}^t \to \mathbb{R}$ as a function of $\widetilde{W_l}$:

$$\widetilde{\phi}_{W_l}(\widetilde{W_l}) := \phi\left(\psi_{W_l}(\widetilde{W_l})\right).$$

For a subset of parameters we define a matrix $\widetilde{D}_l \in \mathbb{R}^{t\times t}$: $\widetilde{D}_l := \|W_l\|_F I_t \in \mathbb{R}^{t\times t}$. Then we define the analog of the product (2) for a subset of t parameters:

$$\widetilde{D}_l \nabla^2 \widetilde{\phi}_{W_l}(\widetilde{W}_l)\widetilde{D}_l \approx \widetilde{Z}_l,$$

where $\widetilde{Z}_l = z_l I_t, z_l > 0$.

E.3 All layers from a single block

If we aim to consider all sub-modules of a single block $i \in \{1, \cdots, B\}$, then we define $\widetilde{W}^i := (\widetilde{W}_{mi+1}, \cdots, \widetilde{W}_{mi+m})$, where $\widetilde{W}_{mi+s} \in \mathbb{R}^t$ is the subset of the first t parameters of the s-th sub-module from the i-th block: $\widetilde{W}_{mi+s} = [\mathcal{R}(W_{mi+s})]_{:t}$, $\widetilde{W}_{mi+s} \in \mathbb{R}^t$. In this case, the perplexity function $\widetilde{\phi}^i : \mathbb{R}^{tm} \to \mathbb{R}$ can be represented the the following way:

$$\widetilde{\phi}^i(\widetilde{W}^i) := \phi\left(\psi_{W_{mi+1}}(\widetilde{W}_{mi+1}), \cdots, \psi_{W_{mi+m}}(\widetilde{W}_{mi+m})\right).$$

Then we define

$$\widetilde{D}^i := Diag(\widetilde{D}_{mi+1}, \dots, \widetilde{D}_{mi+m}) \in \mathbb{R}^{tm \times tm},$$

where $\widetilde{D}_{mi+s} := \|W_{mi+s}\|_F I_t \in \mathbb{R}^{t \times t}$. Then the analog of the product (2) will be

$$\widetilde{D}^i \nabla^2 \widetilde{\phi}^i(\widetilde{W}^i)\widetilde{D}^i \approx \widetilde{Z}^i,$$

where $\widetilde{Z}^i = Diag(\widetilde{Z}_{mi+1}, \dots, \widetilde{Z}_{mi+m}) \in \mathbb{R}^{tm \times tm}$.

E.4 Single sub-module from all blocks

If we aim to consider a single sub-module Q_i for all $i \in \{1, \cdots, B\}$, then we define $\widetilde{Q} := (\widetilde{W}_1, \widetilde{W}_{m+1}, \widetilde{W}_{2m+1}, \cdots, \widetilde{W}_{Bm+1})$, where $\widetilde{W}_{im+1} \in \mathbb{R}^t$ is the subset of the first t parameters of the first sub-module from the i-th block: $\widetilde{W}_{im+1} = [\mathcal{R}(Q_i)]_{:t}$, $\widetilde{W}_{im+1} \in \mathbb{R}^t$. In this case, the perplexity function $\widetilde{\phi}_Q : \mathbb{R}^{Bt} \to \mathbb{R}$ can be represented the the following way:

$$\widetilde{\phi}_Q(\widetilde{Q}) := \phi\left(\psi_{W_1}(\widetilde{W}_1), \psi_{W_{m+1}}(\widetilde{W}_{m+1}), \psi_{W_{2m+1}}(\widetilde{W}_{2m+1}), \cdots, \psi_{W_{Bm+1}}(\widetilde{W}_{Bm+1})\right).$$

Then we define

$$\widetilde{D}_Q := Diag(\widetilde{D}_1, \widetilde{D}_{m+1}, \widetilde{D}_{2m+1}, \dots, \widetilde{D}_{Bm+1}) \in \mathbb{R}^{Bt \times Bt},$$

where $\widetilde{D}_{im+1} := \|Q_i\|_F I_t \in \mathbb{R}^{t \times t}$, Q_i is the first module from the i-th layer. Then the analog of the product (2) will be

$$\widetilde{D}_Q \nabla^2 \widetilde{\phi}_Q(\widetilde{Q})\widetilde{D}_Q \approx \widetilde{Z}_Q,$$

where $\widetilde{Z}_Q = Diag(\widetilde{Z}_1, \widetilde{Z}_{m+1}, \widetilde{Z}_{2m+1}, \dots, \widetilde{Z}_{Bm+1}) \in \mathbb{R}^{Bt \times Bt}$.

E.5 All layers from all blocks

Finally, if we aim to consider all layers and all sub-modules, then we define $\widetilde{W} := (\widetilde{W}_1, \cdots, \widetilde{W}_L)$. The perplexity function $\widetilde{\phi} : \mathbb{R}^{tL} \to \mathbb{R}$ in this case will be

$$\widetilde{\phi}(\widetilde{W}) := \phi\left(\psi_{W_1}(\widetilde{W}_1), \cdots, \psi_{W_L}(\widetilde{W}_L)\right)$$

and $\widetilde{D}^\star := Diag(\widetilde{D}_1, \dots, \widetilde{D}_L) \in \mathbb{R}^{tL \times tL}$, the analog of the product (2) will be

$$\widetilde{D}^\star \nabla^2 \widetilde{\phi}(\widetilde{W})\widetilde{D}^\star \approx \widetilde{Z},$$

where $\widetilde{Z} = Diag(\widetilde{Z}_1, \dots, \widetilde{Z}_L) \in \mathbb{R}^{tL \times tL}$.

E.6 Experimental results

Firstly, let us consider $t = 768$ parameters from only the first layer's $Q_1 \in \mathbb{R}^{768\times768}$. On (Fig. 5a) we can see a diagonal structure of the product $\widetilde{D}_1\nabla^2\widetilde{\phi}_{W_1}(\widetilde{W_1})\widetilde{D}_1 \in \mathbb{R}^{768\times768}$. In this particular case $\widetilde{W_1}$ is the first row of the matrix Q_1.

On the next step, we considered all sub-modules of the first layer – from each matrix $W \in \{Q_1, V_1, K_1, O_1, C_1, S_1\}$, we selected $t = 300$ parameters (Fig. 5b). We can see a clear diagonal structure of the product $\widetilde{D}^1\nabla^2\widetilde{\phi}^1(\widetilde{W}^1)\widetilde{D}^1 \in \mathbb{R}^{1800\times1800}$.

Then we expanded the Hessian computation to include parameters from multiple layers – from each layer, we selected $t = 150$ parameters of the matrix Q_i and repeated this for $i \in \{1, \cdots, B\}$, yielding a product $\widetilde{D}_Q\nabla^2\widetilde{\phi}_Q(\widetilde{Q})\widetilde{D}_Q \in \mathbb{R}^{1800\times1800}$ (Fig. 5c).

Finally, we expanded the Hessian computation to include parameters from all layers and all sub-modules – from each layer W_l, we selected $t = 25$ parameters (Fig. 5d). As before, we can see a clear diagonal structure of the product $\widetilde{D}^\star\nabla^2\widetilde{\phi}(\widetilde{W})\widetilde{D}^\star \in \mathbb{R}^{1800\times1800}$.

In all considered subsets of parameters of OPT-125M we observed a diagonal structure of the product s from Assumption 3. Hence, we have fairly strong reasons to believe that Assumption 3 is satisfied for LLM's.

E.7 Implementation details

To be able to compute the Hessian for only a subset of the network's parameters, we manually defined a perplexity function as a function of the specific subset of parameters. We used this with the PyTorch (Paszke et al., 2019) autograd routines to compute the Hessian quickly and accurately.

Note that Hessian computation induces significant memory consumption when using larger batch sizes. A larger batch size is crucial for accurate perplexity computation, and therefore for accurate Hessian computation (for instance, a batch size of 140 yields a WikiText-2 perplexity for OPT-125M of 27.65, while a batch size of 4 results in a WikiText-2 perplexity of 30.06). To mitigate the memory overflow problem, we modified the perplexity function to exhibit an additive property (Sec. E.8). This means that we can compute the Hessian for the full batch by averaging Hessians, computed over smaller batches. With this adjustment, we were able to use PyTorch's autograd routine to compute the Hessian on a full batch size without encountering memory overflow issues.

E.8 How to compute a Hessian for large batch sizes

The perplexity function is computed by the following sequence of events:

1. Take the input $X \in \mathbb{R}^{b\times l}$ and compute the output of the model by the function $f : \mathbb{R}^{b\times l} \to \mathbb{R}^{b\times l\times n}$, where b is a batch size and l is an output sequence length and n is the size of the embedding space. For OPT-125M, $l = 2048, n = 50272$. Elements of $f(X)$ are called logits and represent the probability for each word to be the next token in the output sequence.

2. Compute the Cross Entropy Loss of the output by the function $g : \mathbb{R}^{b\times l\times n} \to \mathbb{R}^b$,
$$g(f(X)) := \text{nn.CrossEntropyLoss}(f(X)).$$

3. Average the Cross Entropy Loss for all elements from a batch:
$$\bar{c} := \frac{1}{b}\sum_{i=1}^{b} c_i.$$

4. Compute the Perplexity:
$$PPL(\bar{c}) := e^{\bar{c}}.$$

Let us change steps (3) and (4): on the step (3) we will not divide the sum by b, so we define

$$\bar{c}' = \sum_{i=1}^{b} c_i,$$

on the step (4) we will not use the exponential function – instead we will use the identity function:

$$PPL'(\vec{c}') := \vec{c}'. \tag{18}$$

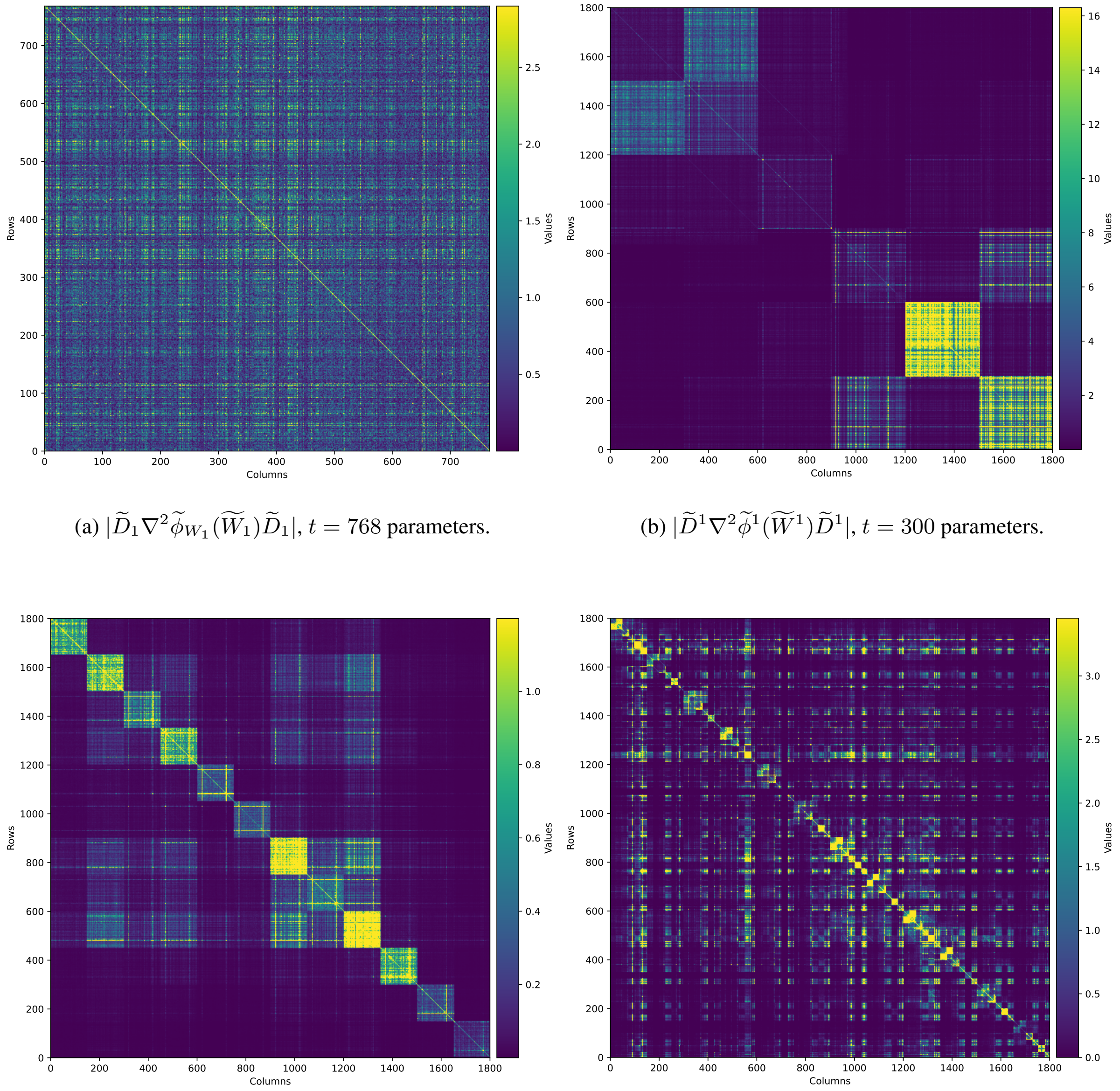

(a) $|\widetilde{D}_1 \nabla^2 \widetilde{\phi}_{W_1}(\widetilde{W}_1)\widetilde{D}_1|$, $t = 768$ parameters.

(b) $|\widetilde{D}^1 \nabla^2 \widetilde{\phi}^1(\widetilde{W}^1)\widetilde{D}^1|$, $t = 300$ parameters.

(c) $|\widetilde{D}_Q \nabla^2 \widetilde{\phi}_Q(\widetilde{Q})\widetilde{D}_Q|$, $t = 150$ parameters.

(d) $|\widetilde{D}^\star \nabla^2 \widetilde{\phi}(\widetilde{W})\widetilde{D}^\star|$, $t = 25$ parameters.

Figure 5: Visual representation of different parts of the product $D^\star \nabla^2 \phi\left(\mathcal{R}(W^\star)\right) D^\star$ for different subsets of parameters. For clarity, we have plotted the absolute values of the entries in all cases to better visualize the magnitude of the elements. For all considered subsets we can clearly see a diagonal structure of the corresponding product. This justifies the Assumption 3.

Theorem 2. *$PPL'(\vec{c}')$ defined in (18) has the additive property. In other words, the perplexity computed for the full batch b will be equal to the sum of perplexities, computed for b subsequent samples.*

Proof. Let us define the functions $\hat{f} : \mathbb{R}^l \to \mathbb{R}^{l \times n}$ and $\hat{g} : \mathbb{R}^{l \times n} \to \mathbb{R}$ to be the same as $f : \mathbb{R}^{b \times l} \to \mathbb{R}^{b \times l \times n}$ and $g : \mathbb{R}^{b \times l \times n} \to \mathbb{R}^b$, but with fixed $b = 1$, so we effectively have a reduction of one dimension.

Since the output $[f(X)]_i \in \mathbb{R}^{l \times n}$ for each sample i from a batch is computed independently, the full output $f(X)$ can be obtained by concatenation of b outputs from $\hat{f}(X_{i,:})$ for $i \in \{1, \cdots, b\}$:

$$f(X) = \left(\hat{f}(X_{1,:}), \cdots, \hat{f}(X_{b,:})\right).$$

The same is true for a Cross Entropy Loss function $g(f(X))$:

$$g(f(X)) = (g(f(X))_1, \cdots, g(f(X))_b) = \left(\hat{g}(\hat{f}(X_{1,:})), \cdots, \hat{g}(\hat{f}(X_{b,:}))\right),$$

hence the equation (19) holds:

$$PPL'(X) = \sum_{i=1}^{b} [g(f(X))]_i = \sum_{i=1}^{b} \hat{g}(\hat{f}(X_{i,:})) \tag{19}$$

where $X_{i,:} \in \mathbb{R}^l$.

In essence, equation (19) means that the perplexity computed for the full batch b will be equal to the sum of perplexities, computed for b subsequent samples.

□

Corollary 2.1. We can compute the Hessian of the perplexity function (18) over large batch of samples by summing up several Hessians, computed on a single sample:

$$\nabla^2 PPL'(g(f(X))) = \sum_{i=1}^{b} \nabla^2 PPL'(\hat{g}(\hat{f}(X_{i,:}))). \tag{20}$$

F Proof of Expected Error

$$\begin{aligned}
&t_l^2(W_l, \mathcal{G}_n^p) := \\
&\quad := \mathrm{E}\left[\|\widehat{W}_l - W_l\|_F^2\right] / \|W_l\|_F^2 = \\
&\quad = \frac{\sum_{i=1}^{D/g} \mathrm{E}\left[\|\widehat{w}_{\{i\}} - w_{\{i\}}\|_F^2\right]}{\sum_{i=1}^{D/g} \|w_{\{i\}}\|_F^2} = \\
&\quad = \frac{\sum_{i=1}^{D/g} s_i^2 \mathrm{E}\left[\|q_{\{i\}}^\dagger - w_{\{i\}}^\dagger\|_F^2\right]}{\sum_{i=1}^{D/g} \|w_{\{i\}}\|_F^2} \approx \\
&\quad \approx \frac{\sum_{i=1}^{D/g} s_i^2 \mathrm{E}_{\mathbf{w}_{\{i\}}^\dagger \sim \mathcal{N}(0,1)}\left[\|q_{\{i\}}^\dagger - w_{\{i\}}^\dagger\|_F^2\right]}{\sum_{i=1}^{D/g} \|w_{\{i\}}\|_F^2} := \\
&\quad := \frac{\sum_{i=1}^{D/g} s_i^2 \cdot g \cdot t^2(\mathcal{G}_n^p)}{\sum_{i=1}^{D/g} \|w_{\{i\}}\|_F^2} = \\
&\quad = t^2(\mathcal{G}_n^p) \frac{\sum_{i=1}^{D/g} \|w_{\{i\}}\|_F^2}{\sum_{i=1}^{D/g} \|w_{\{i\}}\|_F^2} = \\
&\quad = t^2(\mathcal{G}_n^p)
\end{aligned}$$

That is, t_l^2 approximately equals the expected element-wise MSE of rounding the multivariate standard normal distribution to the grid $\mathcal{G}_n^p$

Table 6: Throughput comparison for FLUTE kernels utilizing and omitting the Hadamard transform.

Batch Size	wbits	Throughput with Hadamard, tok/s	Throughput w.o. Hadamard, tok/s
1	2	174	179
	3	150	154
	4	139	143
4	2	687	706
	3	592	607
	4	549	562
16	2	2433	2517
	3	2122	2205
	4	1980	2058

G Processing Hadamard Rotated Matrices

The output $\mathbf{q}^\dagger$ and s of the Algorithm 1 represent a vector to which an RHT has been applied. Additional scale $\frac{1}{\sqrt{g}}$ ensures that this transform preserves the $L2$ norm of the vector is preserved, thus making it a random rotation, controlled by seed ξ, within the rotation groups of size g. This fact opens number of possibilities on how those quantized weights can be processed in the context of LLM inferece.

For the purposes of this section, let us consider a matrix $W \in \mathbb{R}^{N \times N}$ quantized with grid $\mathcal{G}_n^p$ and scales group size g with Algorithm 1 that we want to multiply by some activation matrix $X \in \mathbb{R}^{K \times N}$.

Dequantization. Performing LUT restoration of $\mathbf{w}^\dagger$ from $\mathbf{q}^\dagger$ and $\mathcal{G}_n^p$, then performing a reverse Hadamard rotation in groups and unscaling with s aligns the representation with the original quantized matrix W. This is useful for validation of the representation's correctness, but the time complexity of $O(KN^2 + N^2 \log g)$ it too slow for matrix-vector product operations ($K = 1$) that are crucial for text generation inference.

Rotating Activations. The fact that RHT is a rotation, and that it's controllable by the means of seed ξ allow to use it's scalar product preserving properties to compute matrix-vector or matrix-matrix multiplication fully in the rotated space. More specifically, we can apply RHT to a matrix W in weight groups $W_{\{i\}}$ spanning sequential blocks of output dimension 1 and input dimension g (i.e. $W_{\{1\}} = W$`[0,0:g]`, $W_{\{2\}} = W$`[0,g:2g]`,...). Then, when computing the matrix-matrix product between X and W, we can apply the same RHT (same ξ) to X in the same groups along the input dimension and multiply the rotated matrices directly. This will result in time complexity of $O(KN^2 + KN \log g) = O(KN^2)$. That is, online RHT is asymptotically negligible in terms of time complexity. This approach, among other works, was used by Tseng et al. (2024a). Table 6 showcases the effect of activations Hadamard transforms on end-to-end throughput of Llama-3.1-8B running on an RTX 4090 GPU. The observed difference doesn't exceed four percent.

H Experiment Configurations

H.1 Methods Specifics

- **HIGGS**: for fixed bitwidth we evaluate multiple grid dimensions p by fitting grid size n to match the bitwidth. For 3.25 bits, we use grids with $(p = 2, n = 88)$ and $(p = 3, n = 830)$. For 4.02 bits, we use $(p = 1, n = 16)$ and $(p = 2, n = 256)$. And for 4.25 bits, we use $(p = 1, n = 19)$ and $(p = 2, n = 361)$. We use scaling groups of size 1024 for all HIGGS experiments.

- **Dynamic HIGGS**: for dynamic bitwidth we only use FLUTE grids and CH8. We benchmark FLUTE kernel speed through its custom vLLM integration.

- **Normal Float (NF):** for ≈ 4 bits configurations we use the grid from `bitsandbytes` library. We use `group_size=64` (default) for 4.25 bits and `group_size=1024` (same as HIGGS) for 4.02 bits. For

≈ 3 bits we obtain the entropy-optimal grid and implement quantization-dequantization ourselves. We do not use double quantization. We benchmark kernel speed through its vLLM integration.

- **Abnormal Float (AF):** we reuse the grid generation process of (Yoshida, 2023) from the corresponding repository. We apply it to 3 and 4 bit grids of group size 64 and 1024, resulting in 3.02, 3.25, 4.02 and 4.25 bit configurations.
- **HQQ:** we use the official implementation of Half-Quadratic Quantization. We use `group_size=64` for nbits.25 bits and `group_size=1024` for nbits.02 bits, where nbits$\in \{2, 3, 4, 8\}$. We disable double quantization for fair comparison with other methods that don't use it.
- **GPTQ:** we use GPTQ implementation from the autogptq library. We set `bits=3,group_size=64` for 3.25 bits, `bits=4,group_size=1024` for 4.02 bits and `bits=4,group_size=64` for 4.25 bits. We always `clip=True,mse=1` for MSE-optimal grid clipping. We benchmark MARLIN kernel speed through its vLLM integration.
- **AQLM:** we re-report the perplexity metric specifically for the w/o fine-tuning version of AQLM from the corresponding paper's ablation study (Egiazarian et al., 2024). We benchmark kernel speed through its vLLM integration.
- **QuIP#:** we re-report the perplexity metric specifically for the w/o fine-tuning version of QuIP# from the corresponding paper's ablation study (Tseng et al., 2024a).
- **QTIP#:** we re-report the perplexity metric specifically for the w/o fine-tuning version of QTIP from the corresponding paper's ablation study (Tseng et al., 2024b). We re-report the metrics selectively for the 3INST grid for 2 and 4 bits and for the 1MAD grid for 3 bits. We use the end-to-end generation speed measurement scripts provided in the official repository.

I Additional Evaluations

Method	wbits	Wiki2	ArcC	ArcE	PiQA	Wino	HellaS	Avg	MMLU
FP16	16.00	8.644	31.31	65.53	74.54	60.54	47.73	55.93	32.04
AF	3.25	19.750	25.85	50.46	66.10	54.46	37.64	46.90	25.46
NF	3.25	17.761	24.15	49.83	66.70	53.99	38.57	46.65	26.70
HQQ	3.25	17.965	26.28	52.90	68.01	55.56	38.76	48.30	25.52
HIGGS (p=2)	3.25	13.196	26.96	56.10	69.97	54.06	40.79	49.58	24.62
HIGGS (p=3)	3.25	12.423	29.10	56.78	69.37	58.33	41.00	50.91	25.87
HIGGS (p=4)	3.25	**12.185**	28.41	57.53	69.80	57.85	41.86	**51.09**	**28.01**
HIGGS (dyn data-free)	3.25	11.082	30.03	59.68	71.27	58.17	43.20	52.47	27.27
HIGGS (dyn)	3.25	**10.949**	30.38	60.14	70.89	57.70	43.37	**52.49**	**28.24**
AF	4.02	10.183	30.29	61.95	73.39	58.56	44.59	53.76	**28.28**
NF	4.02	10.703	28.07	60.90	73.12	57.77	44.47	52.87	25.53
HQQ	4.02	26.516	25.43	49.75	64.15	53.83	36.96	46.02	26.26
HIGGS (p=1)	4.02	10.167	31.83	62.58	72.96	58.88	45.19	54.29	26.37
HIGGS (p=2)	4.02	9.735	32.25	64.48	74.16	57.77	46.28	**54.99**	28.12
HIGGS (p=3)	4.02	**9.641**	29.18	61.36	72.63	59.59	45.45	53.64	26.95
HIGGS (dyn data-free)	4.00	9.520	31.40	63.34	74.27	60.22	45.79	**55.00**	27.83
HIGGS (dyn)	4.00	**9.375**	31.66	63.09	73.94	59.43	46.26	54.87	**27.87**
AF	4.25	9.543	30.63	63.47	73.88	59.67	46.17	54.76	30.29
NF	4.25	9.575	30.89	62.37	74.21	60.54	45.58	54.72	28.83
HQQ	4.25	9.646	32.25	62.42	73.56	59.83	46.20	**54.85**	29.52
HIGGS (p=1)	4.26	9.600	30.29	62.12	72.69	59.83	46.10	54.20	28.36
HIGGS (p=2)	4.26	9.336	30.89	64.18	73.56	59.35	46.18	54.83	28.79
HIGGS (p=3)	4.25	**9.299**	30.29	63.43	73.29	60.77	46.32	54.82	**30.91**
HIGGS (dyn data-free)	4.25	9.341	31.91	63.51	74.37	59.91	46.07	55.15	**29.44**
HIGGS (dyn)	4.25	**9.205**	31.57	63.59	74.27	59.91	46.68	**55.20**	28.29

Table 7: Quantization evaluations for Llama3.2 1b

Method	wbits	Wiki2	ArcC	ArcE	PiQA	Wino	HellaS	Avg	MMLU
FP16	16.00	6.979	42.15	74.45	76.71	69.93	55.29	63.71	56.07
AF	3.25	10.81	33.11	65.61	71.65	64.40	47.41	56.44	42.00
NF	3.25	10.04	37.29	70.37	73.94	65.35	49.45	59.28	44.71
HQQ	3.25	9.252	36.35	68.14	74.21	64.33	50.01	58.61	44.42
HIGGS (p=2)	3.25	9.156	35.75	67.89	74.32	64.96	50.16	58.61	46.76
HIGGS (p=3)	3.25	8.711	37.37	71.59	74.37	66.30	50.62	60.05	46.82
HIGGS (p=4)	3.25	**8.669**	37.88	70.58	73.18	67.32	51.40	**60.07**	**48.94**
HIGGS (dyn data-free)	3.25	8.007	39.25	71.72	74.97	67.64	51.76	**61.07**	**51.09**
HIGGS (dyn)	3.25	**7.979**	38.40	71.97	75.14	67.25	52.42	61.03	50.59
AF	4.02	7.697	41.13	73.36	76.39	68.67	53.81	62.67	53.08
NF	4.02	7.819	39.68	73.57	76.01	67.56	53.17	62.00	51.13
HQQ	4.02	12.57	34.73	68.77	72.74	64.09	47.66	57.60	36.89
HIGGS (p=1)	4.02	7.695	41.30	73.99	75.95	67.80	53.35	62.48	53.01
HIGGS (p=2)	4.02	7.507	41.64	73.86	76.33	68.27	54.11	**62.84**	53.82
HIGGS (p=3)	4.02	**7.464**	40.44	71.76	76.66	68.82	53.87	62.31	**54.20**
HIGGS (dyn data-free)	4.00	7.399	39.76	73.19	76.22	67.96	53.70	62.17	54.37
HIGGS (dyn)	4.00	**7.295**	41.04	73.27	76.44	68.51	53.75	**62.60**	**54.43**
AF	4.25	7.365	40.61	73.15	76.88	68.27	54.43	62.67	54.53
NF	4.25	7.395	41.98	73.86	76.71	68.75	54.35	**63.13**	54.51
HQQ	4.25	7.351	42.75	72.77	76.93	68.82	53.89	63.03	53.33
HIGGS (p=1)	4.26	7.459	40.19	72.31	76.12	67.96	53.97	62.11	53.43
HIGGS (p=2)	4.26	7.339	38.23	69.82	76.22	68.59	54.23	61.42	54.44
HIGGS (p=3)	4.25	**7.306**	40.53	73.65	76.39	69.06	53.95	62.72	**54.54**
HIGGS (dyn data-free)	4.25	7.266	40.02	73.44	76.01	69.53	54.01	62.60	**54.66**
HIGGS (dyn)	4.25	**7.216**	41.21	73.40	76.17	69.06	54.22	**62.81**	54.63

Table 8: Quantization evaluations for Llama3.2 3b

Method	wbits	Wiki2	ArcC	ArcE	PiQA	Wino	HellaS	Avg	MMLU
FP16	16.00	6.497	51.71	81.78	79.92	73.80	59.12	69.26	68.20
AF	3.25	8.848	43.69	74.92	77.75	69.61	53.52	63.90	57.51
NF	3.25	8.663	43.00	75.51	77.48	71.11	54.73	64.37	58.42
HQQ	3.25	8.273	46.59	77.23	77.97	71.19	55.70	65.73	59.41
HIGGS (p=2)	3.25	7.765	44.80	75.97	77.53	72.69	56.58	65.51	61.32
HIGGS (p=3)	3.25	7.659	49.74	80.35	77.64	71.67	56.59	67.20	62.26
HIGGS (p=4)	3.25	**7.469**	48.72	78.66	79.65	72.77	56.31	**67.22**	**63.83**
HIGGS (dyn data-free)	3.25	7.351	48.63	78.49	78.51	70.48	56.76	66.58	63.79
HIGGS (dyn)	3.25	**7.204**	47.78	79.12	78.89	72.53	57.27	**67.12**	**64.36**
AF	4.02	7.107	50.51	79.84	79.43	73.64	57.69	68.22	65.28
NF	4.02	7.084	49.74	80.35	79.43	73.95	58.14	68.32	65.59
HQQ	4.02	9.393	48.29	77.48	77.04	71.59	55.50	65.98	60.21
HIGGS (p=1)	4.02	7.013	49.15	80.18	79.65	72.53	57.70	67.84	65.64
HIGGS (p=2)	4.02	6.901	49.15	81.27	79.87	73.24	58.20	68.35	**65.98**
HIGGS (p=3)	4.02	**6.833**	50.17	81.82	79.98	72.77	58.59	**68.67**	65.77
HIGGS (dyn data-free)	4.00	6.835	50.68	80.60	79.60	73.40	58.17	68.49	66.05
HIGGS (dyn)	4.00	**6.720**	50.68	81.48	79.87	73.40	58.55	**68.80**	**66.41**
AF	4.25	6.758	51.96	80.68	79.16	72.85	58.57	68.65	66.41
NF	4.25	6.882	51.62	80.98	79.27	73.72	58.41	68.80	**67.21**
HQQ	4.25	6.777	50.51	81.02	79.33	73.80	58.37	68.61	66.44
HIGGS (p=1)	4.26	6.838	50.51	80.35	79.71	72.85	58.47	68.38	66.40
HIGGS (p=2)	4.26	**6.736**	53.75	81.82	80.09	74.03	58.24	**69.59**	67.14
HIGGS (p=3)	4.25	6.741	51.37	81.10	79.71	73.32	58.79	68.86	66.97
HIGGS (dyn data-free)	4.25	6.783	50.94	81.31	80.09	74.03	58.33	68.94	**66.86**
HIGGS (dyn)	4.25	**6.664**	51.28	81.61	79.92	74.59	58.81	**69.24**	66.32

Table 9: Quantization evaluations for Llama3.1 8b Instruct

Method	wbits	Wiki2	ArcC	ArcE	PiQA	Wino	HellaS	Avg	MMLU
FP16	16.00	2.541	60.67	87.25	83.13	79.64	66.48	75.43	78.51
AF	3.25	102350	51.54	81.52	80.85	75.14	62.54	70.32	60.53
NF	3.25	41.76	54.78	81.57	80.85	76.40	63.22	71.36	63.42
HQQ	3.25	4.057	57.17	84.30	81.23	77.82	64.21	**72.95**	75.32
HIGGS (p=2)	3.25	4.297	54.44	84.09	81.34	70.88	63.76	70.90	73.44
HIGGS (p=3)	3.25	4.023	57.08	84.55	81.56	67.48	64.14	70.96	75.10
HIGGS (p=4)	3.25	**3.792**	55.72	83.96	82.15	72.06	65.34	71.85	**75.77**
HIGGS (dyn data-free)	3.25	3.675	58.45	85.48	81.61	79.40	64.39	73.87	76.36
HIGGS (dyn)	3.25	**3.466**	57.68	85.52	82.15	78.93	65.23	**73.90**	**76.98**
AF	4.02	513.5	21.16	25.46	53.16	59.83	52.34	42.39	25.71
NF	4.02	2084	20.73	25.51	52.67	52.17	27.34	35.68	23.47
HQQ	4.02	4.023	55.63	83.21	80.85	74.51	62.21	71.28	74.67
HIGGS (p=1)	4.02	3.115	58.70	85.35	82.54	77.82	65.83	74.05	77.27
HIGGS (p=2)	4.02	2.986	60.15	86.28	82.64	78.85	66.20	**74.83**	77.59
HIGGS (p=3)	4.02	**2.956**	59.64	86.07	82.97	77.90	65.98	74.51	**77.80**
HIGGS (dyn data-free)	4.00	3.133	60.15	86.15	82.75	78.61	66.04	74.74	77.68
HIGGS (dyn)	4.00	**2.827**	60.24	86.74	82.70	79.64	66.17	**75.10**	**78.24**
AF	4.25	2.982	58.96	86.32	83.03	80.27	65.89	**74.89**	77.11
NF	4.25	3.065	57.25	86.28	82.70	78.14	66.04	74.08	78.12
HQQ	4.25	2.873	60.67	87.04	82.75	77.98	65.75	74.84	**78.47**
HIGGS (p=1)	4.26	2.935	58.53	86.07	82.32	77.27	65.83	74.00	77.62
HIGGS (p=2)	4.26	2.852	59.30	86.62	82.21	78.85	66.12	74.62	78.00
HIGGS (p=3)	4.25	**2.834**	60.49	86.36	82.59	78.53	66.02	74.80	77.70
HIGGS (dyn data-free)	4.25	2.956	60.67	86.74	82.81	78.77	66.05	75.01	**78.14**
HIGGS (dyn)	4.25	**2.787**	60.92	86.32	83.03	79.87	66.35	**75.30**	78.09

Table 10: Quantization evaluations for Llama3.1 70b. We don't quantize attention's value layer for the first transformer block of the model in non-dynamic setups.

Method	wbits	Wiki2	ArcC	ArcE	PiQA	Wino	HellaS	Avg	MMLU
FP16	16.00	6.128	47.70	80.51	78.67	72.93	60.02	67.97	74.13
AF	3.25	7.542	46.59	79.38	77.37	68.19	55.27	65.36	67.16
NF	3.25	7.588	44.28	76.94	77.42	67.72	55.34	64.34	68.27
HQQ	3.25	7.247	46.84	76.01	78.13	67.25	56.68	64.98	69.58
HIGGS (p=2)	3.25	6.808	46.59	77.78	78.78	71.19	57.97	66.46	70.90
HIGGS (p=3)	3.25	6.732	46.25	77.78	78.73	70.72	57.97	66.29	71.41
HIGGS (p=4)	3.25	**6.669**	48.04	79.55	78.07	71.59	58.08	**67.06**	**71.73**
HIGGS (dyn data-free)	3.25	6.604	47.61	79.17	78.40	72.30	57.56	67.01	71.26
HIGGS (dyn)	3.25	**6.566**	48.21	79.34	78.62	71.27	57.64	**67.01**	**71.41**
AF	4.02	6.538	45.31	77.86	77.91	71.82	58.28	66.24	72.23
NF	4.02	6.538	47.61	79.59	78.35	69.85	58.98	66.88	72.35
HQQ	4.02	7.767	44.88	76.22	77.26	68.98	55.33	64.53	70.72
HIGGS (p=1)	4.02	6.407	47.35	79.71	78.51	70.40	58.60	66.92	72.78
HIGGS (p=2)	4.02	6.359	48.81	80.30	79.00	72.22	58.68	**67.80**	72.97
HIGGS (p=3)	4.02	**6.325**	47.27	79.97	78.67	72.14	59.10	67.43	**73.39**
HIGGS (dyn data-free)	4.00	6.334	48.89	79.67	78.78	70.72	58.87	**67.39**	72.58
HIGGS (dyn)	4.00	**6.291**	47.70	78.75	78.84	71.67	59.04	67.20	**73.10**
AF	4.25	6.352	48.29	79.46	78.18	71.27	58.83	67.21	73.29
NF	4.25	6.340	46.67	79.63	78.35	71.19	59.00	66.97	73.44
HQQ	4.25	6.358	46.93	79.97	78.89	71.11	59.38	67.26	73.32
HIGGS (p=1)	4.26	6.343	48.81	79.08	78.56	73.01	58.64	67.62	73.67
HIGGS (p=2)	4.26	6.298	46.76	79.17	78.84	73.16	59.05	67.40	73.30
HIGGS (p=3)	4.25	**6.278**	47.70	79.92	78.13	73.16	59.20	**67.62**	**73.86**
HIGGS (dyn data-free)	4.25	6.282	48.21	79.71	78.78	70.56	58.85	67.22	**73.32**
HIGGS (dyn)	4.25	**6.255**	48.72	80.22	78.84	70.88	59.01	**67.53**	73.28

Table 11: Quantization evaluations for Qwen2.5 7B